INORGANIC CHEMISTRY
FRONTIERS

RESEARCH ARTICLE

View Article Online
View Journal | View Issue

Cite this: *Inorg. Chem. Front.*, 2025, **12**, 7304

New encapsulated bis-cyclometalated Ir(III) complexes with very potent anticancer PDT activity†

Cristina Bermejo-Casadesús, ‡[a] Carlos Gonzalo-Navarro, ‡[b] Juan Angel Organero,[c] Ana María Rodríguez,[d] Lucía Santos,[e] Elisenda Zafon,[a] Joao Carlos Lima,[f] Artur J. Moro,[f] Mònica Iglesias,[g] Pedro Tavares,[h,i] Daniel Martínez,[b] Blanca R. Manzano, *[b] Anna Massaguer *[a] and Gema Durá *[b]

Photodynamic therapy (PDT) has emerged as a promising approach for cancer treatment, due to its ability to reduce side effects. In the search for luminescent iridium $[Ir(C^N)_2(N^N)]^+$ complexes with high ability to generate ROS (reactive oxygen species) under irradiation, we employed C^N ligands with high π-expansion (pbpz (4,9,14-triazadibenzo[*a*,*c*]anthracene), **1**, or pbpn (4,9,16-triazadibenzo[*a*,*c*]naphthacene), **3**) that should lead to long excited state lifetimes. The photophysical properties were significantly influenced by the degree of C^N ligand π-expansion. Complex **1** exhibited a long fluorescence lifetime, matching the triplet lifetime observed in TAS, suggesting delayed fluorescence. In contrast, the additional ring in complex **3** generated two near-HOMO orbitals, increasing the excited state's LC character and reducing spin–orbit coupling (SOC) and intersystem crossing (ISC). They exhibited a notable ability to generate $^1O_2$ and $O_2^{\bullet-}$. TD-DFT studies nicely explained the differentiated photophysical properties. Both complexes exhibited significant phototoxicity against human cancer cells in both monolayer and multicellular spheroids models, with complex **1** exhibiting a higher effect. They effectively photogenerated intracellular ROS, including $O_2^{\bullet-}$. The mitochondrial accumulation of **1** and its disruption of mitochondrial functions were verified. Wound healing and clonogenic assays demonstrated their potential as antimetastatic agents. In general, complexes' encapsulation significantly facilitated their cellular accumulation and increased photocytotoxic indexes, with **NP1** achieving one of the lowest IC_{50} values reported in iridium chemistry. Furthermore, the nanoparticles showed good anticancer activity even in 3D models. Thus, **1** and **3** and especially **NP1** show great promise as type I and II PDT agents with theragnostic potential.

Received 18th March 2025,
Accepted 1st July 2025

DOI: 10.1039/d5qi00775e

rsc.li/frontiers-inorganic

[a]*Universitat de Girona, Departament de Biologia, Facultat de Ciències, Maria Aurelia Capmany 40, 17003 Girona, Spain. E-mail: anna.massaguer@udg.edu*
[b]*Universidad de Castilla-La Mancha, Departamento de Química Inorgánica, Orgánica y Bioquímica- IRICA, Facultad de Ciencias y Tecnologías Químicas, Avda. Camilo José Cela, 10, 13071 Ciudad Real, Spain. E-mail: gema.dura@uclm.es, blanca.manzano@uclm.es*
[c]*Universidad de Castilla-La Mancha, Departamento de Química Física, Facultad de Ciencias Ambientales y Bioquímicas and INAMOL, 45071 Toledo, Spain*
[d]*Universidad de Castilla-La Mancha, Departamento de Química Inorgánica, Orgánica y Bioquímica- IRICA, Escuela Técnica Superior de Ingenieros Industriales, Avda. Camilo José Cela, 3, 13071 Ciudad Real, Spain*
[e]*Universidad de Castilla-La Mancha, Departamento de Química Física, Facultad de Ciencias y Tecnologías Químicas, Avda. Camilo José Cela, s/n, 13071 Ciudad Real, Spain*
[f]*Universidade NOVA de Lisboa, LAQV-REQUIMTE, Departamento de Química, Faculdade de Ciências e Tecnologia, 2829-516 Caparica, Portugal*
[g]*Universitat de Girona, Departament de Química, Facultat de Ciències, Maria Aurelia Capmany 40, 17003 Girona, Spain*
[h]*Associate Laboratory i4HB – Institute for Health and Bioeconomy, NOVA School of Science and Technology, Universidade NOVA de Lisboa, 2829-516 Caparica, Portugal*
[i]*UCIBIO – Applied Molecular Biosciences Unit, Department of Chemistry, NOVA School of Science and Technology, Universidade NOVA de Lisboa, 2829-516 Caparica, Portugal*

†Electronic supplementary information (ESI) available: Experimental section, NMR spectra, ESI+ MS spectra, HPLC traces, X-ray diffraction, analysis of π–π stacking by ^1H NMR spectroscopy, stability and photostability, photophysical properties, transient absorption spectroscopy (TAS) measurements, ROS generation, computational studies, synthesis and characterization of nanoparticles, hemolytic activity, NADH oxidation, internalization analyses. Biological Studies Raw Data. CCDC 2431327–2431329 for complexes **1**, **2** and **4**. For ESI and crystallographic data in CIF or other electronic format see DOI: https://doi.org/10.1039/d5qi00775e

‡Both authors have contributed equally to the work.

1. Introduction

Photodynamic therapy (PDT)[1–4] has emerged as a promising approach for cancer treatment because of its ability to reduce side effects, circumventing one of the main problems limiting the effectiveness of chemotherapy. This technique is a minimally invasive therapeutic modality that has gained significant attention for its ability to selectively target and eradicate cancer cells with spatio-temporal control. PDT relies on the use of a photosensitizer (PS) that, upon light activation, increases the cytotoxic effect in cancer cells through the generation of reactive oxygen species (ROS). This ROS generation is divided into two pathways depending on the type of interaction between the PS and the molecules of the medium. Type I PDT in which an electron transfer mechanism to O_2 or other oxygen-containing species renders different ROS, among them the superoxide anion radical ($O_2^{\bullet-}$), which not only acts as an oxidant to destroy cancer cells, but can also suffer a series of cascade bioreactions leading to species such as hydroxyl radicals ($HO^{\bullet}$) or H_2O_2, which are also cytotoxic. In type II PDT, an energy transfer mechanism to the fundamental oxygen ($^3O_2$) generates singlet oxygen ($^1O_2$), a very reactive and toxic species.[5,6] Type II processes are more dependent on O_2 concentration, and thus PSs acting by type I or both are more adequate for hypoxic tumours. One measure of the potential of a PS is the phototoxic index (PI), which is the ratio of the cytotoxicity in the dark and after irradiation ($PI = IC_{50,dark}/IC_{50,light}$).

There are a number of PSs in clinical use that have been approved either globally or in specific countries for different types of cancer.[7–9] The majority are organic agents with a tetrapyrrolic scaffold, which suffer, among other problems, prolonged retention in tissues, photobleaching and a small Stokes shift that greatly increases the interference between excitation and emission.[10] Metal-based tetrapyrrolic derivatives are under clinical trials or approved, as in the case of TOOKAT, a palladium complex.[8] In the last decades attention has been paid to d^6 transition metal complexes, which offer easy ligand modification, potential redox features and versatile photochemical and photophysical properties with intense absorptions in the visible region.[11–14] Specifically, the triplet state, which has a longer lifetime than the singlet state and facilitates PSs reactions with O_2, is typically more prevalent in metal complexes.[13] Interesting results have been obtained with osmium,[15] rhenium[16] and ruthenium.[17,18] It is noteworthy that the ruthenium derivative TLD1433, developed by McFarland, is undergoing clinical trials.[19]

Among the various PSs reviewed in the literature, cyclometalated Ir(III) complexes have shown exceptional promise due to their unique and tunable photophysical properties, favourable absorption characteristics, large Stokes shifts and robust stability and photostability under physiological conditions. Additionally, the triplet excited states of Ir(III) complexes are highly sensitive to molecular oxygen and high quantum yields for ROS generation are observed.[20–24] Moreover, it is common for these derivatives to target mitochondria, giving them high potential in PDT cancer therapy.[25,26] These characteristics make Ir(III) complexes potent candidates for enhancing the efficacy of PDT. Besides, octahedral bis(cyclometalated) complexes of Ir(III) are remarkable for their intrinsic luminescence properties and are used as cellular imaging reagents and biomolecular probes.[27]

Studies have shown that compounds with long excited state lifetimes are more efficient at producing ROS, exhibit high singlet oxygen ($^1O_2$) quantum yields, and have demonstrated significant photocytotoxicity *in vitro*.[28,29] It is known that the greater the $^3\pi\pi^*$ character of the triplet excited state, the longer the T_1 lifetime.[30] Interestingly, utilizing ligands with extended π-systems reduces the energy of the ligand-centered (LC) $^3\pi\pi^*$ state to below or near that of the ^{3}MLCT state, significantly increasing the $^3\pi\pi^*$ character and lifetime of the T_1 state.[28,31–33] The use of π-extended ligands also favors absorption at longer wavelengths in the visible and near-infrared regions, which is advantageous for deeper tissue penetration and minimizing damage to surrounding healthy tissue. This approach has been successfully used, reaching PDT activity in ruthenium chemistry[28,34–39] and also in iridium derivatives of N_6 type,[40,41] half-sandwich[42] and derivatives of stoichiometry $[IrCl(C\hat{}N)(N\hat{}N\hat{}N)]^+$.[43] The use of π-extending ligands has also been applied to bis(cyclometalated) species of the type $[Ir(C\hat{}N)_2(N\hat{}N)]^+$ where the π-extension has mainly focused on the N^N ligand,[44–54] but it has also been explored for the C^N ligand[25,55,56] or both.[57–64] Some complexes demonstrated superior ROS generation capabilities, making them effective at inducing phototoxicity in cancer cells. With some exceptions,[55,65,66] in general, the π-extension used in C^N ligands consists of the incorporation of a fused benzene to the phenylpyridinate (ppy) ligand, usually in the pyridine fragment. In their excellent work, Vilar *et al.* have studied,[60] by a high-throughput approach, the photocytotoxicity of a wide library of iridium compounds. From DFT calculations, they concluded that, although the N^N ligand also influenced the outcome of the derivatives, the C^N ligand dominated the electronic structure properties of the complexes. In her research on bis(cyclometalated) iridium complexes, McFarland discovered that the degree of π-conjugation in the diimine ligand predominantly influences the $^1\pi,\pi^*$ transitions observed in their UV-vis absorption spectra and that the π-conjugation of the cyclometalating ligand primarily determines the nature and energies of the lowest singlet and emitting triplet excited states.[67] Recently, we have reported the first case of half-sandwich cyclometalated iridium complexes with PDT activity using the C^N ligands pbpz (4,9,14-triazadibenzo[*a*,*c*]anthracene) or pbpn (4,9,16-triazadibenzo[*a*,*c*]naphthacene) (Fig. 1).[42] Considering all these precedents, we decided to focus on studying the π-extension of the C^N ligand and synthesize derivatives of the type $[Ir(C\hat{}N)_2(bpy)]^+$ (bpy = 2,2′-bipyridine) using the pbpz and pbpn C^N ligands, which exhibit a remarkable π-extension. A potential advantage of the targeted derivatives over the half-sandwich complexes with the same ligands is the expected luminescence, which enables a theragnosis effect, combining both therapeutic and diagnostic functionalities in cancer treatment.

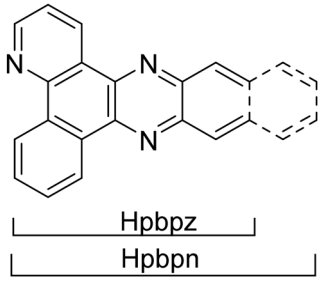

Fig. 1 Structure of the proligands Hpbpz and Hpbpn.

Despite their potential, the clinical application of Ir(III) complexes in PDT faces significant challenges related to their delivery and bioavailability.[68] To overcome these limitations, encapsulation of PSs within nanoparticles has been proposed as a viable strategy.[69–71] Nanoparticles offer several advantages as drug delivery systems, including improved solubility, protection from premature degradation and the enhanced permeability and retention (EPR) effect,[72,73] thus increasing their accumulation in cancerous tissues[74] and minimizing systemic toxicity. Cross-linked polymeric nanoparticles have shown enormous potential as carriers due to their low toxicity and biocompatibility.[75] Since these nanoparticles do not establish dynamic equilibria, they retain their structure even at low concentrations, and they are preserved in the bloodstream longer than self-assembled systems. This favours their accumulation in tumours.[76] A wide variety of molecules such as proteins, DNA, drugs, hydrophobic and hydrophilic molecules, have been encapsulated in this type of system.[77–80]

In this study, we report the synthesis and characterization of two new biscyclometalated Ir(III) complexes with π-extended C^N ligands and their encapsulation into polymeric nanoparticles. The use of this type of ligand has allowed long lifetimes of the excited states to be obtained, and a remarkable generation not only of $^1O_2$ but also of $O_2^{\bullet-}$. The photophysical properties were highly dependent on the type of ligand, a fact that was excellently explained by TD-DFT studies. The complexes exhibited photodynamic efficacy under blue light irradiation, resulting in mitochondrial damage and an antimetastatic effect. Encapsulation of the complexes significantly enhanced their cellular uptake and photodynamic activity. Notably, one of the nanoparticles exhibited, under irradiation, one of the highest values of cytotoxicity found in iridium chemistry (IC_{50} = 0.86 nM).

2. Results and discussion

2.1. Synthesis and characterization of complexes

Two new biscyclometalated Ir(III) complexes of general formula $[Ir(C^N)_2(N^N)]^+$ (C^N = pbpz, 4,9,14-triazadibenzo[*a*,*c*]anthracene; or pbpn, 4,9,16-triazadibenzo[*a*,*c*]naphthacene; N^N = 2,2′-bipyridine) have been prepared (Scheme 1). The proligands were synthesized using a literature procedure (Scheme 1).[18] These ligands were previously used in octahedral polypyridine Ru(II) complexes,[18] $[IrCl(C^N)(N^N^N)]^+$ derivatives[81] and half-sandwich Ir(III) complexes[42] exhibiting excellent PDT behaviour.

The synthesis of the biscyclometalated Ir(III) dimer **D1** and the equivalent with the pbpn ligand was attempted by the conventional method, that implies the use of a ethylene glycol monomethyl ether : water (3 : 1) mixture.[82,83] However, this approach was unsuccessful, possibly because the proligands are not sufficiently nucleophilic to react with the Ir(III) center due to electron delocalization. To improve the reaction conditions, microwave techniques were employed. However, only Hpbpz was successfully cyclometalated in these conditions and **D1** was obtained. Subsequently, the cationic complex **1** was prepared by abstraction of the chloride using $AgOSO_2CF_3$ and coordination of the N^N ligand, followed by anion exchange with NH_4PF_6.

To achieve the analogous complex with the pbpn ligand, a different approach was employed. In this case, benzo[*h*]quinoline-5,6-dione was first cyclometalated to the Ir(III) center using 2-methoxyethanol : water (3 : 1) mixture under microwave irradiation leading to the formation of the dimer **D2**. Subsequently, the N^N ligand was coordinated mediated by the chloride abstraction with $AgOSO_2CF_3$, followed by anion exchange with NH_4PF_6 (formation of **2**). Finally, 2,3-diaminonaphtalene was condensed to the cyclometalated benzo[*h*]quinoline-5,6-dione to obtain **3**.

The complexes were obtained in moderate yields (38–41%) as black, yellow or red solids. The complexes **1–3** were fully characterized by elemental analysis, ^1H, $^{13}C\{^1H\}$ and $^{19}F\{^1H\}$ NMR spectroscopy, including ^1H–^1H gCOSY, ^1H–^{13}C gHSQC and ^1H–^{13}C gHMBC and mass spectrometry (Fig. S1–S27†). Moreover, the crystal structures of **1**, **2** and the adduct formed after reaction of **D2** with DMSO, **4** (Scheme 1), were also solved by single crystal X-ray diffraction. The HPLC traces were also obtained for complexes **1** and **3** (Fig. S28 and S29†).

Complexes **1** and **2** exhibited good solubility in polar solvents such as dimethyl sulfoxide (DMSO) and chlorinated solvents as well as in *N*,*N*-dimethylformamide (DMF), methanol or acetonitrile. Complex **3** exhibited solubility in DMSO and DMF. Complexes **1–3** were poorly soluble in aqueous media. However, the cationic complexes were soluble in water provided that a small amount of another solvent, such as DMSO or DMF was added. Thus, nontoxic amounts of DMSO were used in the biological experiments to assist dissolution.

In the ^1H NMR spectra, the lack of a signal for the proton of the metalated carbon (H^7) and the shift of the resonances for the protons of pbpz and pbpn in the complexes with respect to those for the corresponding proligands (Hpbpz and Hpbpn) corroborates the coordination of the C^N ligands to the metal centre. The resonances were fully assigned by means of ^1H–^1H COSY experiments and considering the different coupling constants expected in the pyridyl ring.[42,84] The strong shielding of the proton adjacent to the metallated carbon (H^{12}) of both the pbpz or pbpn ligands due to the effect of the ring current anisotropy of the pyridine ring of the other C^N ligand

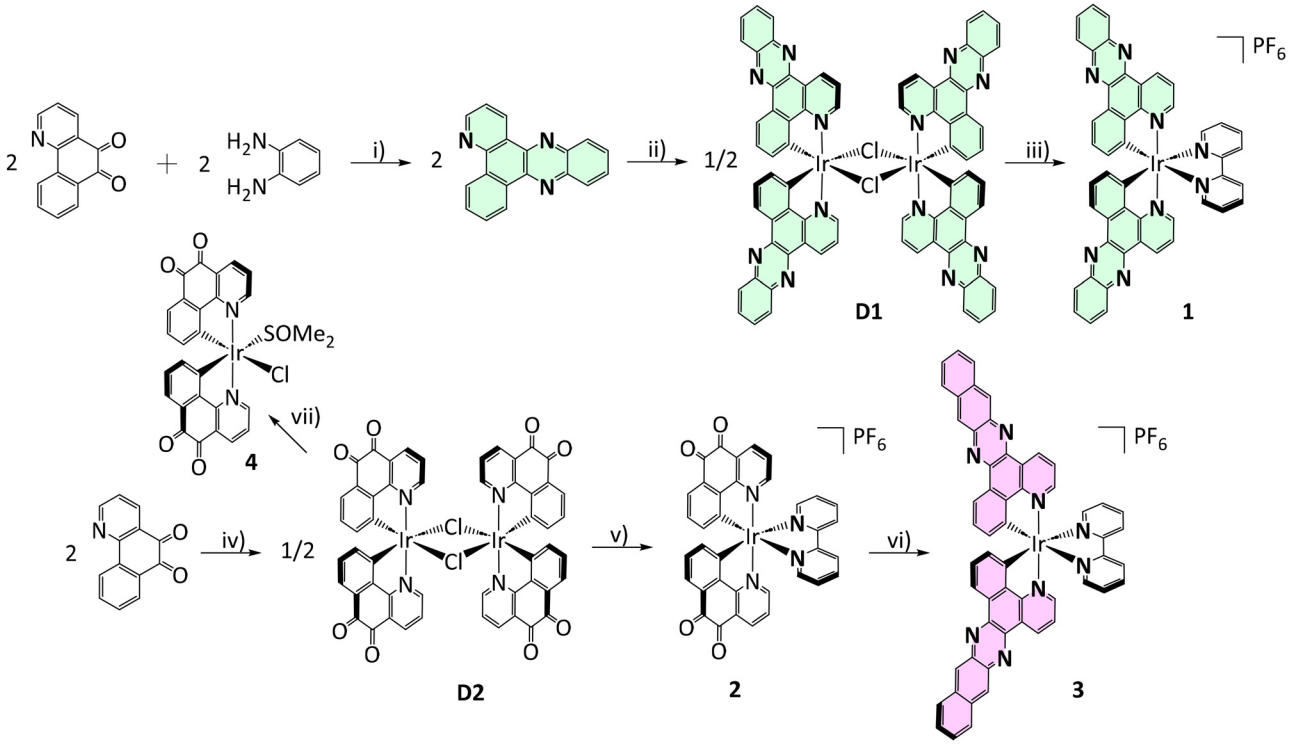

Scheme 1 Synthesis of ligands and complexes presented in this paper. (i) EtOH, reflux, 4 h. (ii) $IrCl_3{\cdot}3H_2O$, diglyme/H_2O (3 : 1), MW, 220 °C, 10 min. (iii) bpy, $AgOSO_2CF_3$, DCM/MeOH (2 : 1), reflux, 24 h and NH_4PF_6, room temperature, 1 h. (iv) $IrCl_3{\cdot}3H_2O$, 2-methoxyethanol/H_2O (3 : 1), MW, 150 °C, 10 min. (v) bpy, $AgOSO_2CF_3$, DCM/MeOH (2 : 1), reflux, 36 h and NH_4PF_6, room temperature, 1 h. (vi) 2,3-Diaminonaphtalene, EtOH, reflux, 4 h. (vii) DMSO, room temperature.

is noticeable, as it is clearly observed in the structure of **1** determined by X-ray diffraction described below.[85,86] It was also possible to assign most of the $^{13}C\{^1H\}$ NMR resonances through ^1H–^{13}C gHSQC and ^1H–^{13}C gHMBC experiments.

2.2. Solid-state characterization by X-ray diffraction and analysis of π–π stacking

The molecular and crystal structures of complexes **1**, **2** **[OSO_2CF_3]** and **4** were determined by X-ray diffraction. The corresponding ORTEP diagram of complex **1** is shown in Fig. 2. The ORTEP diagrams of complexes **2[OSO_2CF_3]** and **4** are shown in Fig. S30.† The methods used to obtain single crystals are detailed in the Experimental section. Selected bond distances and angles are gathered in Table S1.† The crystallographic data are provided in Table S2.† The three compounds exhibit a distorted octahedral geometry with the two nitrogen atoms of the C^N ligands in a relative *trans* disposition, as expected.[87–89] The Ir–C and Ir–N distances of the C^N ligand are about 2 Å while those involving the N atoms of the N^N ligand are a bit longer because of the *trans* influence of the carbon atoms.[26,90,91] The iridium atoms are chiral but both enantiomers are observed in a single crystal.

Concerning non-covalent interactions, besides the cation–anion coulombic attractions and hydrogen bonding, it is worth noting the presence of π–π interactions involving the C^N ligands. In the case of **1**, the molecules are assembled

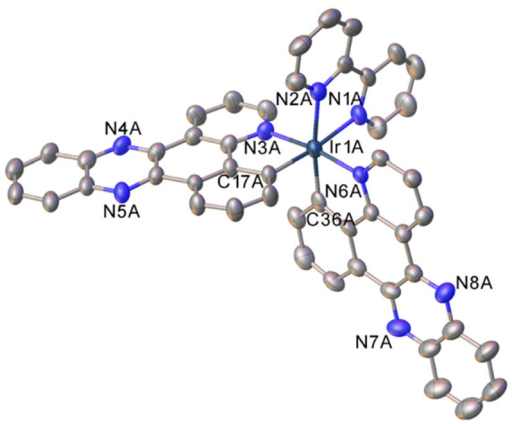

Fig. 2 ORTEP diagram of cation of complex **Δ 1**. Ellipsoids are at the 30% probability level. Hydrogen atoms and PF_6^- anion have been omitted for clarity.

into trimers by weak π–π interactions (Fig. S31†). There are two trimers in the asymmetric unit; one contains three Δ enantiomers (trimer Δ) and the other three Λ enantiomers (trimer Λ) (Fig. S32†). Molecules of different trimers are further packaged by other π–π interactions (Fig. S33†). Other examples of π–π interactions in cationic complexes involving a N^N ligand similar to pbpz[49,92–95] and in neutral and cationic complexes

of formula $[Cp^*Ir(C^N)L]^{0/+}$ with pbpz and pbpn[42] have been reported.

Considering the π–π stacking interactions observed in the solid state, it was decided to ascertain whether this interaction was also present in solution. Thus, complexes **1** and **3** were studied by ^{1}H NMR spectroscopy at different concentrations. The existence of the π–π stacking interaction on increasing the concentration could be proved by observing the shielding of specific ring protons due to the influence of the ring current from the adjacent aromatic moieties.[96,97] In addition, this study could provide information about the regions that are mostly involved in the interaction. The differences in chemical shifts of the C^N aromatic protons for the most diluted and concentrated solutions in DMSO-d_6 are provided in Table S3.† The corresponding sets of spectra are given in Fig. S34 and S35.† Although nearly all C^N aromatic protons suffer concentration-dependent changes in chemical shift, the effect of shielding when the concentration is increased depends on the specific compound and on the position of the proton on the ligand. Higher $\Delta\delta$ values were found for complex **3** that contains pbpn, the more π-expansive ligand, probably due to a more efficient π-stacking interaction. Besides, the protons mostly affected are those situated in the central region of the ligands (see Fig. S36†).

Stability, photostability and aggregation studies (NMR, UV-vis and DLS). The stability of the new Ir(III) complexes was studied by ^{1}H NMR spectroscopy in the dark and under blue light irradiation (470 nm, 51.4 mW cm^{-2}) in DMSO-d_6 due to the poor water solubility of the complexes (Fig. S37–S40, and Table S4†). Both compounds were highly stable during the irradiation time used in the biological studies. To simulate the conditions in the biological experiments, the stability in biological medium (DMEM) was studied by UV-vis spectroscopy in the dark and under blue light irradiation (Fig. S41 and S42†). As can be seen, the UV-vis spectra of both complexes were unchanged in the dark after 48 h, revealing the stability of the complexes in these conditions. Under blue light irradiation, some changes were observed for both complexes. The UV-vis spectra seem to evolve into a new species, as has been previously observed for other compounds with this type of π-expansive ligand. It was proposed that light favours an aggregation process.[42]

In order to ascertain if the compounds aggregate spontaneously and confirm the light-induced aggregation of the complexes, a Dynamic Light Scattering (DLS) experiment was performed for solutions of both complexes at 1.0×10^{-4} M in water (10% DMSO) mixture before and after 1 h of blue light exposure. The average hydrodynamic diameter of particles of **1** and **3** before irradiation was 79 and 117 nm, respectively (Fig. S43†). These results indicate that the compounds form nanoaggregates in the presence of a high percentage of water, which is favoured by the hydrophobicity of the π-extended ligands and the polarity of water, as has been seen for other Ir(III) complexes in the literature.[98] In addition, after 1 h of blue light irradiation, the average hydrodynamic diameter of both compounds increased. The values for **1** and **3** were 378 and 323 nm, respectively (Fig. S43†). Therefore, light irradiation induces an increase in the aggregation of the particles, resulting in larger aggregates. Although it is not a common process, other examples of light-induced aggregation have been reported.[99–101]

2.3. Photophysical properties

UV-vis absorption spectra. The UV-vis absorption spectra of complexes **1** and **3** were recorded in degassed acetonitrile at 1.0×10^{-5} M at 25 °C (Fig. S44,† and Table 1). Their spectra are relatively similar. Both spectra show two intense bands below 350 nm with a red shift of about 30 nm for **3** with respect to **1**. They are assigned to π–π* transitions of the ligands (see the spectra of the proligands in Fig. S45†). Moreover, the spectra exhibit two additional bands of lower intensity at longer wavelengths, centred at around 390 and 440 nm for **1** and at 414 and 480 nm for **3**. The simulated TD-DFT absorption spectra for both complexes (Fig. S77 and S78†) and the calculated electronic transitions (see below) indicate that these bands primarily correspond to a mixture of metal-to-C^N ligand charge transfer (d → π*, ^{1}MLCT) and C^N ligand-to-ligand charge transfer (π → π*, ^{1}LLCT) transitions in both series. There are

Table 1 Photophysical properties of complexes **1** and **3** and proligands Hpbpz and Hpbpn in acetonitrile, unless otherwise stated

Comp.	λ/nm ($\varepsilon \times 10^{-4}$/M^{-1} cm^{-1})	ε^a (M^{-1} cm^{-1}) (460, 515, 635 nm)	λ_{em} (λ_{exc})/nm	Φ_{em} [b]	τ_{em}/ns (contrib.)[c]	k_r (s^{-1} × 10^{-6})[d]	k_{nr} (s^{-1} × 10^{-7})[d]	τ_{em}/ns (aerat.)[e]	τ_{em}/ns (degas.)[e]	φ_Δ [f]
1	272 (15.9), 302 (6.5), 358 (2.8), 390 (2.0), 438 (1.2)	6290 920 10	596 (440)	0.32	150 (14%) 440 (86%)	0.80	0.17	360	3450	0.59
3	246 (8.2), 300 (13.2), 320 (8.7), 340 (7.1), 394 (2.2), 414 (2.5), 478 (1.5)	8510 5790 190	550 (420)	0.02	0.60 (25%) 13.1 (75%)	2.0	9.8	180	2160	0.49
Hpbpz	308 (1.8), 350 (1.2), 366 (2.0), 388 (2.3)	n.m.	508 (412)	n.m.	n.m.	n.m.	n.m.	n.m.	n.m.	n.m.
Hpbpn	302 (3.4), 376 (0.5), 396 (1.1), 420 (1.5)	n.m.	544 (400)	n.m.	n.m.	n.m.	n.m.	n.m.	n.m.	n.m.

[a] In water (1% DMSO). [b] The Φ_{em} in degassed acetonitrile was determined using $[Ir(ppy)_2(bpy)]PF_6$ as reference (φ_{em} = 0.0707).[102] [c] In aerated acetonitrile solutions. [d] Radiative decay rate $k_r = \Phi/\tau$ and nonradiative decay rate $k_{nr} = (1 - \Phi)/\tau$. [e] Excited-state lifetimes in acetonitrile measured by TAS. [f] The ϕ_Δ ($^1O_2$ generation quantum yield) in water (10% DMSO) under blue light irradiation (470 nm) was determined using $[Ru(bpy)_3]^{2+}$ as reference (ϕ_Δ = 0.18).[103] n.m. = not measured.

also absorption tails that extend until 500 and 550 nm for **1** and **3**, respectively. The red-shift observed in the absorption spectrum of **3** reflects the strong electron-withdrawing ability and extended π-conjugation of the benzo-quinoxaline ligand, as was observed before.[42] This fact enhances its light-harvesting capability and increases its sensitivity to light sources that can penetrate deeper into tissues.

In order to better understand the photophysical properties of the complexes in biological media, the UV-vis spectra were also recorded in water (1% DMSO) (Fig. 3). Comparing with the spectra recorded in acetonitrile, all the absorption bands in water were red-shifted (Table S5†). In water, the absorption tails extended until 540 and 580 nm for **1** and **3**, respectively, promoting absorption of longer wavelengths in biological experiments, which is desirable for a PS. See in Table 1 the values of absorptivity at the wavelengths used in the biological studies.

Emission spectra. The photoluminescence spectra of both complexes were initially recorded in solutions of dry deoxygenated acetonitrile (1.0×10^{-5} M) at 25 °C upon excitation at λ = 420–440 nm (Fig. S44† and Table 1). Both compounds emitted at *ca.* 550–600 nm upon excitation at the lower energy band of the absorption spectrum. The emission spectrum for complex **1** exhibited one band with λ_{max} at 596 nm and a shoulder at around 550 nm. The emission spectrum for complex **3** showed one emission band centred at around 550 nm, similar to the emission spectrum of Hpbpn (Fig. S46†). However, the emission spectrum of **1** was quite different to the spectrum of Hpbpz (Fig. S46†), with the main band red-shifted with respect to the proligand, and also red-shifted with respect to the emission of **3**. The photoluminescence quantum yields (Φ_{em}) recorded for these complexes were also quite different (Table 1). Complex **1** exhibited a good quantum yield (0.32) while the value for complex **3** was very low (0.02), which indicates that an additional non-radiative pathway is in action for **3**, while absent in **1**. This additional non-radiative pathway does not seem to be intersystem crossing, since the proximity in the values of φ_Δ of **1** and **3** (Table 1) indicate close quantum yields of triplet formation for **1** and **3**.

The emission properties of the complexes were also studied in aerated water (1% DMSO, 1.0×10^{-5} M) at 25 °C upon excitation at λ = 422–470 nm (Fig. 3, and Table S5†). In aqueous solution, complex **1** remains highly emissive, which makes it a good candidate as a bioimaging agent. However, complex **3** is hardly emissive. In both cases the emission bands undergo a red shift with respect to the results in acetonitrile, with a more pronounced displacement for complex **1** (λ_{max} = 632 nm). This may be related to the stated aggregation process[104] as confirmed in the following experiment.

The possible aggregation effect in the emission properties was evaluated in H_2O : DMSO mixtures with different water fractions (f_w) (Fig. S47†). As can be seen in Fig. S48,† both complexes showed an aggregation-caused quenching (ACQ) process. The effect is stronger in the case of **3**, probably due to the larger π-conjugation of the C^N ligand. Interestingly, the quenching process is only partial in the case of **1**. Concerning the position of the emission bands, the red-shifting is small in the case of complex **3** but for **1** there is a notable red-shifting upon aggregation.

The weak fluorescence of **3** may be due to its aggregation in aqueous media, driven by the greater hydrophobicity and stronger π–π interactions of the pbpn ligand. In addition, the expected reduction in spin–orbit coupling (SOC) in this compound (see below) favours fluorescence as the predominant radiative deactivation pathway.

Luminescence lifetimes. Time-correlated single-photon counting (TC-SPC) was performed to analyse the decay times associated with the luminescence. Iridium complexes are known to present multiple exponential decays due to the decay of singlet and triplet states at the same emission wavelength.[105] The multiexponential profiles of the luminescence decays are also observed in this case (Fig. S49†), but the decay times of complexes **1** and **3** present clear differences in time scale. **1** presents luminescence decays that are best fitted with a sum of two exponentials. The longer decay time, 440 ns, is responsible for 86% of the observed emission. **3** also presents luminescence decays that are best described as a sum of two exponentials. However, the longest decay time, 13.1 ns, which accounts for 75% of the luminescence, is much shorter (see below for the lifetimes obtained from TAS).

Transient absorption spectroscopy (TAS) measurements. Transient absorption spectra of both compounds measured at room temperature in acetonitrile solutions (Fig. S50†) between 280 and 600 nm display negative and positive optical density values yielding the same lifetime for both the negative regions (ground state depletion) and positive regions (transient state formation) of the transient absorption spectrum, which confirms that the disappearance of the transient state and recovery of the ground state are connected (Table 1). The optical density variations at both wavelengths decay to zero at longer times, indicating that no other species is being formed in significant amounts throughout the experiments (Fig. S51†), *i.e.*, there is no evidence for photochemistry arising from the

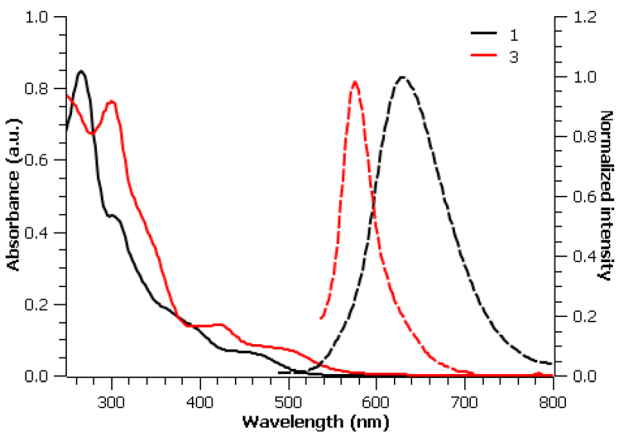

Fig. 3 UV-vis absorption and emission spectra of complexes **1** and **3** in water (1% DMSO).

observed transients. Furthermore, the solutions were degassed by bubbling Argon until saturation (~20 minutes), and the transients were once more acquired, yielding excited state lifetimes around one order of magnitude higher (Table 1). These results suggest that the observed transients are of triplet nature, which are strongly quenched in the presence of O_2. UV-vis spectra acquired before and after laser flash photolysis on both complexes are identical, confirming that there is no photochemistry occurring in these conditions (Fig. S52†).

The long luminescence lifetimes, similar to the triplet lifetimes observed in TAS, point to a contribution of delayed fluorescence in the fluorescence emission of **1**. The luminescence lifetime values obtained for **3** are much shorter than the ones obtained from TAS and we conclude that the contribution of delayed fluorescence is thus considerably less in this compound.

TAS was also performed in aqueous solution (1% DMSO) of **1** (15 μM). Transients at selected wavelengths, namely 270 nm (for monitoring ground-state depletion) and 560 nm (for monitoring transient absorption) were acquired (Fig. S53†) and compared with the transients obtained in acetonitrile. It can be seen that the transients of **1** are greatly diminished in water, when compared with acetonitrile (around ten-fold decrease in the initial absorbance of the transient), while the lifetime of the transient is not significantly changed (Table 2). These findings indicate that the initial concentration of T_1 is greatly diminished in water, because either S_1 or higher triplet states are undergoing photochemistry that competes efficiently with the formation of T_1 in aqueous solution.

ROS generation. The ability of Ir(III) complexes to generate ROS was investigated through four different methods: quenching of the triplet state by O_2, the 9,10-anthracenediyl-bis (methylene) malonic acid (ABDA) test for $^1O_2$ production, the dihydrorhodamine 123 (DHR123) assay for $O_2^{\bullet-}$ production and EPR spectroscopy with specific radical spin-traps.

The relationship between the triplet state quenching of Ir(III) complexes by O_2 bubbling and ROS formation is significant because it largely relies on energy and/or electron transfer processes, as has been previously described.[106–108] The result of these transfer processes is the generation of singlet oxygen and different oxygen radicals. As can be seen in Fig. S54,† in acetonitrile, the quenching of emission by O_2 is several times higher in complex **1** than in complex **3**. In part, this is related to the triplet contribution to the emission (delayed fluorescence) of complex **1**, which is much smaller in the case of complex **3**. The significant decrease in the emission of complex **1** in the presence of oxygen confirms the quenching of its triplet state. Therefore, complex **1** is expected to be a good photosensitizer.

Singlet oxygen generation was studied using the ABDA assay in water (10% DMSO) to assess its performance under conditions more representative of those used in bioassays. In this experiment, $^1O_2$ generation quantum yields (φ_Δ) were quantified monitoring the decrease in the ABDA absorbance by UV-vis spectroscopy with the irradiation for 3.5 minutes. The experiment was performed in dark conditions and under blue light irradiation (470 nm, 51.4 mW cm^{-2}). $[Ru(bpy)_3]^{2+}$ was used as reference (φ_Δ = 0.18 in water).[109] First, the stability of ABDA was confirmed under blue light irradiation (Fig. S55†). In the presence of the Ir(III) complexes and $[Ru(bpy)_3]^{2+}$, a decrease in the absorption bands of the probe (360, 378 and 400 nm) over time was only observed upon blue light irradiation (Fig. S56–58†). In dark conditions, the spectrum of ABDA remained unaltered. The φ_Δ values of the two new complexes were calculated from the slopes obtained for ABDA consumption (Fig. S59†). Although there is not much difference, **1** exhibited the highest φ_Δ (0.59) while **3** exhibited a slightly lower value (0.49) (Table 1). This result indicates that the quantum yields for triplet formation and the efficiency of energy transfer to O_2 are comparable for both complexes. Despite the luminescence of complex **3** being less affected by the presence of O_2, it is still a good photosensitizer.

Generation of $O_2^{\bullet-}$ was studied by the DHR123 assay in water (0.2% DMSO) monitoring the emission change of the probe by fluorescence spectroscopy with the irradiation for 30 seconds. The non-emissive DHR123 probe is oxidized by the photogenerated $O_2^{\bullet-}$ into the fluorescent rhodamine 123, with a maximum emission at 526 nm. As for $^1O_2$ studies, the experiment was carried out in dark conditions and upon blue light irradiation (470 nm, 51.4 mW cm^{-2}) using $[Ru(bpy)_3]^{2+}$ as reference. In dark conditions (Fig. S60†) or under blue light without any complex (Fig. S61†), no oxidation of the probe was detected. Upon blue light irradiation, with complexes **1**, **3** or $[Ru(bpy)_3]^{2+}$, $O_2^{\bullet-}$ generation was confirmed by the increased emission of the oxidized rhodamine 123 (Fig. S62 and S63†). The relative rates are in order of **1** ≫ **3** > $[Ru(bpy)_3]^{2+}$. Moreover, ascorbic acid and sodium azide were used as scavengers for $O_2^{\bullet-}$ and $^1O_2$, respectively, to determine their relative contributions to the oxidation of DHR123 (Fig. S64 and S65†). As expected, the oxidation of DHR123 was inhibited, and the increase in its fluorescent signal was significantly reduced in the presence of ascorbic acid, while sodium azide had no measurable effect. These results confirm that both complexes generate $O_2^{\bullet-}$ under light irradiation in aqueous solution. Notably, the triplet state of complex **1** exhibits a greater ability to act as an $O_2^{\bullet-}$ photosensitizer, in contrast to $^1O_2$ photosensitization where the φ_Δ values were comparable for both compounds.

The generation of $O_2^{\bullet-}$ for **1** was also verified in acetonitrile with the DHR123 assay (Fig. S66†). The superoxide production was higher in water than in acetonitrile, as is clearly seen in Fig. S67.† This is aligned with the TAS results, which showed that the transients of complex **1** were significantly reduced in

Table 2 Excited-state lifetimes and initial optical densities for **1** in water (1% DMSO) and acetonitrile, measured with laser flash photolysis

		OD (t = 0)	
Solvent	Lifetime (ns)	270 nm	560 nm
Water (1% DMSO)	371	−0.0071	0.0031
Acetonitrile	367	−0.0727	0.0335

water compared with acetonitrile (Table 2). The initial concentration of the lowest triplet state T_1 is greatly diminished in aqueous solution, which accounts for the reduced contribution of $O_2^{\bullet-}$ to the oxidation of DHR123 in this solvent mixture. Moreover, this provides strong evidence for an additional photochemical process involving higher triplet states that compete with T_1 formation (see below), specifically leading to $O_2^{\bullet-}$ generation. These results underscore complex **1** as a particularly promising PDT agent, as it implies a type I mechanism that, while enhanced by oxygen, can also function independently of it. This makes it especially useful against cells in hypoxic microenvironments.[110]

Finally, EPR experiments on **1** under dark and irradiated (365 nm) conditions were conducted in acetonitrile, in the presence of two radical specific spin-traps: 2,2,6,6-tetramethylpiperidine (TEMP) and 5,5-dimethyl-1-pyrroline-*N*-oxide (DMPO). In the case of TEMP, it reacts with $^1O_2$ to yield 2,2,6,6-tetramethylpiperidine-*N*-oxide radical (TEMPO), characterized by a distinct three-line signal.[111–113] This radical is thermodynamically and kinetically stabilized and easily accumulates in solution. The signal was readily detected after irradiation (Fig. S68A†), supporting the presence of $^1O_2$ in the sample. The reaction of $O_2^{\bullet-}$ with the nitrone DMPO leads to the formation of the DMPO–OOH spin adduct, which gives rise to a characteristic EPR signal consisting of a quartet due to hyperfine splitting from the nitroxide nitrogen and the adjacent β-hydrogen.[114] Contrary to TEMPO, this spin adduct radical presents a rapid decay due to spontaneous rearrangement and degradation. The short lifetime limits the detection window. As such, *in situ* irradiation was carried out, and the resulting EPR spectrum confirmed the presence of $O_2^{\bullet-}$ in solution (Fig. S68B†).

2.4. Polymeric nanoparticles

We decided to explore the possibility of encapsulating the complexes into crosslinked polymeric nanoparticles with the aim of improving the cellular internalization and evaluating their behaviour as anticancer agents in PDT. The preparation of the nanoparticles involved two main steps: the synthesis of copolymers (Scheme S1†) and the crosslinked step to produce the nanoparticles *via* covalent bonds (Fig. 4).

Synthesis of copolymers. The copolymers used in this work were prepared by RAFT (Reversible Addition Fragmentation chain Transfer) polymerization, which was used on account of its features such as versatility, high compatibility with different solvents and monomers and experimental simplicity to obtain polymers with narrow M_w.[115] Polyethyleneglycol (PEG)-based monomers were selected in order to obtain polymers with higher solubility in protic solvents. In addition, it protects against non-specific interactions with the proteins in blood, avoiding aggregation.[116]

The chain transfer agent (CTA) used in both polymerizations was 2-cyano-2-propyl dodecyl trithiocarbonate due to its suitability to acrylates and methacrylates. The polymers were purified by dialysis. Two polymers were obtained containing amine and carboxylic groups, which were used to generate cross-linked network *via* amide bonds (Scheme S1†). Random copolymer **P1** was obtained *via* copolymerization of poly(ethyleneglycol) methyl ether methacrylate (PEGMA) and 2-aminoethyl methacrylate, which was used with the BOC protecting group as monomer (BOC-aminoethylMA). This monomer was

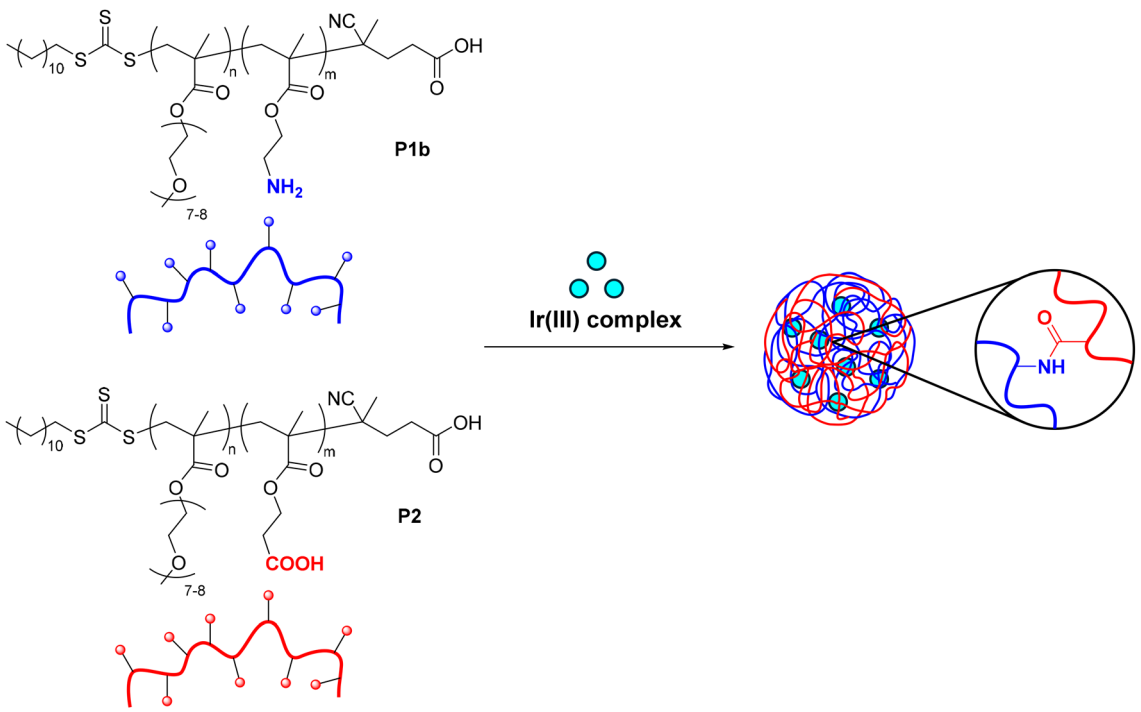

Fig. 4 Schematic formation of the NPs presented in this work with Ir(III) complexes encapsulated.

prepared according to the literature.[117] In a second step, the protecting group was removed with TFA (trifluoroacetic acid), to obtain **P1b** with the amine groups. Random copolymer **P2** was obtained *via* copolymerization of PEGMA and 2-carboxyethyl acrylate (CEA) (Scheme S1†). The conversion of the polymerizations was calculated by ^{1}H NMR using trioxane as standard and was found to be around 87 and 90% for **P1** and **P2**, respectively (Table S6†). The three polymers were characterized by ^{1}H NMR (Fig. S69–S71†).

Synthesis and characterization of nanoparticles. Crosslink experiments were performed between copolymers **P1b** and **P2** in the presence of the coupling agent 1-ethyl-3-(3-dimethylaminopropyl)carbodiimide (EDC) to yield polymeric nanoparticles *via* covalent amide bond formation, as a result of coupling of amine and carboxylic groups (Fig. 4). Equimolar dilute solutions of copolymers were mixed in water, and the corresponding amount of coupling agent was added dropwise while stirring. It was expected that these nanoparticles could encapsulate drug payloads, and thus, encapsulate the Ir complexes. A similar procedure was performed to obtain the nanoparticles in the presence of the complexes (Table S7†).

The nanoparticles were characterised by DLS, affording hydrodynamic diameters between 150–200 nm with a good polydispersity index (PDI) (Table S7 and Fig. S72†). This structure provides a stable aqueous suspension of the nanoparticles with good biological properties, such as long circulation in the bloodstream and specific accumulation in the acidic tumour microenvironment. The size of the nanoparticle without encapsulated drug was found to be 146 nm, showing that the size of the nanoparticle does not change significantly with the encapsulation of drugs. SEM images of the nanoparticles showed their spherical morphology (Fig. S73†).

Nanoparticles **NP1** and **NP3** (containing compound **1** or **3**, respectively) were analysed by UV-vis spectroscopy (Fig. S74†) in water. The spectra are relatively similar to those of complexes **1** and **3** in aqueous solution. The encapsulation of the drugs into the nanoparticles improved the solubility of the complexes but did not affect the UV-vis absorption spectra. The emission properties of the nanoparticles were also studied in water at 25 °C upon excitation at λ_{exc} = 422–470 nm. As observed for the free complex, **NP1** showed a highly emissive behaviour, which makes it a good candidate for a bioimaging agent (Fig. S75†). However, similar to complex **3**, **NP3** was hardly emissive. This confirmed that encapsulation of complexes did not affect their photophysical properties.

The amount of complex encapsulated in each nanoparticle was confirmed by ICP-MS, with values of drug loading of 23.319 and 27.560 μM for **NP1** and **NP3**, respectively (Table S7†). These values of drug loading could be considered low compared with other nanocarriers of Ir complexes,[74] possibly on account of the high lipophilicity of the Ir(III) complexes and the absence of any surfactant in the synthesis method. The drug uploading values of these nanoparticles were 5.8 and 7.7%, respectively. Despite the low Ir content, we decided to evaluate these nanoparticles and their effect on cytotoxicity and cellular uptake.

2.5. Theoretical calculations

In order to gain a better understanding of the significant differences in the photophysical properties of the complexes **1** and **3**, time-dependent density functional theory (TD-DFT) calculations were performed for both the singlet and triplet excited states of these compounds. A comprehensive method for comparing the X-ray crystallography and theoretical geometries involves superimposing the two structures and calculating the root-mean-square deviation (RMSD) of atomic positions (Fig. S76†). For compound **3**, the X-ray structure was not obtained. The corresponding RMSD value corresponding to the overlap for those structures of **1** is 0.131 Å. This indicates that the experimental and the obtained theoretical geometries are quite similar. No significant differences were observed in the length values of both structures. The primary difference arises from slight distinctions in the orientation of the planes of the aromatic fragments, which are influenced by the crystal packing effect in the structure determined by X-ray diffraction but not in the obtained theoretical structures.

The corresponding fragmental contributions of each molecular fragment to the molecular orbitals (Fig. S79†) corresponding to complexes **1** and **3** were obtained by a Milliken population analysis (Table 3 and Fig. 5). The energy of the HOMO orbitals is comparable between the two compounds because their main contributions are similarly derived from the atomic orbitals of the iridium atom (45%), and the benzene fragment (38% and 40%) as well as the pyridine moiety (9% and 8%) in the pbpz and pbpn ligands, respectively. It is important to highlight that for **3**, both HOMO−1 and HOMO−2 orbitals are almost isoenergetic with the HOMO orbital. Notably, the majority of their contribution (88%) originates from the benzo-quinoxaline moiety, and these orbitals are characterized by their π nature. The formation of a near-HOMO orbital centred on the benzo-quinoxaline fragment due to the introduction of the pbpn ligand has also been observed in our previous work with $[Cp^*Ir(C\hat{}N)L]^+$ complexes.[42] In the case of compound **3**, the introduction of two pbpn ligands results in the presence of two near-HOMO orbitals of this nature. The nearly isoenergetic character of these orbitals indicates that the electrons in the HOMO orbital can be delocalized across these three orbitals, thereby enhancing their delocalization over the π system of the ligand and further contributing to its stability. Interestingly, such type of orbital is missing in compound **1**, where the HOMO−1 closely resembles and shares energy equivalence with the HOMO−3 of compound **3**, with a major contribution, in both compounds, of fused benzene and minor contributions of pyridine and quinoxaline(**1**)/benzo-quinoxaline(**3**) moieties. Regarding the LUMO and LUMO+1, they are predominantly isoenergetic in both compounds, with their primary locations being on the benzo-quinoxaline fragment in compound **3**, resembling HOMO−1 and HOMO−2 orbitals, and on the quinoxaline moiety in compound **1**. Besides, the addition of an extra fused benzene ring in **3** has the effect of lowering the LUMO level by extending the π-conjugation system, which leads to greater

Table 3 Energies in electron volts (E/eV) and main fragmental contributions (percentage values within brackets) to some molecular orbitals of **1** and **3** obtained at the TD-DFT (SMD, acetonitrile)/6-31G(d,p)//SDD level

	E/eV		**1**	**3**
Orbital	**1**	**3**	Fragmental contributions (%)	Fragmental contributions (%)
LUMO+5	−1.27	−1.29	Bpy (52) Py (15) Q (14) Bz (13) Ir (5)	Bpy (53) Py (17) Bq (13) Bz (11)
LUMO+4	−1.80	−1.78	Py (60) Bz (17) Q (17) Ir (5)	Py (62) Bz (16) Bq (15) Ir (6)
LUMO+3	−1.83	−1.81	Py (63) Bz (17) Q (13)	Py (64) Bz (17) Bq (12)
LUMO+2	−2.17	−2.17	Bpy (93)	Bpy (93)
LUMO+1	−2.41	−2.69	Q (76) Py (16) Bz (8)	Bq (80) Py (12) Bz (7)
LUMO	−2.47	−2.73	Q (73) Py (16) Bz (10)	Bq (77) Py (13) Bz (9)
HOMO	−5.59	−5.60	Ir (45) Bz (40) Py (8)	Ir (45) Bz (38) Py (9) Bq (6)
HOMO−1	−6.17	−5.65	Bz (57) Py (22) Q (17)	Bq (88) Bz (7)
HOMO−2	−6.22	−5.65	Ir (32) Bz (27) Q (25) Py (13)	Bq (88) Bz (7)
HOMO−3	−6.25	−6.19	Q (34) Bz (31) Ir (22) Py (11)	Bz (58) Bq (23) Py (15)
HOMO−4	−6.39	−6.29	Ir (44) Q (29) Py (14) Bz (9)	Ir (58) Py (14) Bz (12) Bq (10) Bpy (6)
HOMO−5	−6.45	−6.35	Ir (52) Q (24) Py (12) Bz (7) Bpy (6)	Ir (56) Py (17) Bz (14) Bq (8) Bpy (6)

Ir: iridium, Q: quinoxaline, Bq: benzo-quinoxaline, Bz: fused benzene, Py: pyridine and Bpy: bipyridine.

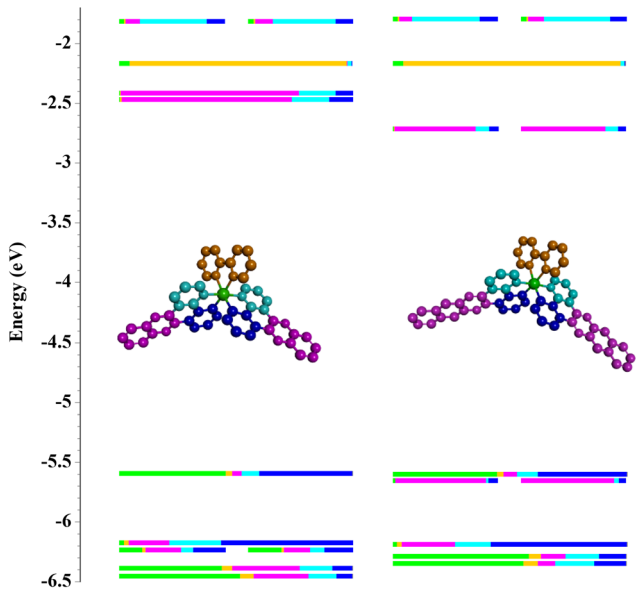

Fig. 5 Optimized ground state structures for **1** (left) and **3** (right) obtained from TD-DFT [(B3LYP/SDD for Ir(III)) and (6-31g** for C,H,N)] with SMD (CH_3CN). For the sake of clarity, the hydrogen atoms are not shown, and each molecular fragment has been assigned a colour code. The length of each colour bar is proportional to the percentage contribution of the corresponding coloured moiety to each molecular orbital. Colour codes for bars and molecular fragments: iridium atom (green), quinoxaline or benzo-quinoxaline (pink), fused benzene (navy blue), pyridine (blue), bipyridine (brown).

delocalization of the LUMO and LUMO+1. This extended conjugation leads to a greater delocalization of the π and π* orbitals, resulting in a narrowing of the energy gaps between the frontier molecular orbitals. This extension results in a red shift in the absorption compared with compound **1**.

To gain a better understanding about the behaviour of the studied compounds in their electronic excited states, the vertical excitation energies were calculated along with the orbitals involved in these excitations and their relative contributions to singlet and triplet excited states (Table 4). In compound **3** the difference in energy between $S_0 \rightarrow S_{1-4}$ was ≤ 0.07 eV. This indicates that the excitations to these singlet excited states are very close in energy due to excitations involving multiple closely spaced occupied orbitals (HOMO, HOMO−1, and HOMO−2) to a pair of nearly degenerate unoccupied orbitals (LUMO and LUMO+1), as shown in Table 4. The transitions $S_0 \rightarrow S_1$, $S_0 \rightarrow S_2$, and $S_0 \rightarrow S_4$ exhibit a combination of metal-to-ligand charge transfer (MLCT), ligand-to-ligand charge transfer (LLCT), and ligand-centred (LC) characteristics. Conversely, the transition $S_0 \rightarrow S_3$ is primarily characterized as ligand-centred (LC). The close energy spacing between these excited states enhances the probability of internal conversion (IC), as the excitation energy can be efficiently transferred to vibrational modes and it could lead to strong vibronic coupling between states, giving a broad absorption spectrum where the electronic transitions can borrow intensity from each other.[118,119]

As far as compound **1** is concerned, the electronic states S_1–S_4 exhibit mixed MLCT/LLCT characteristics. This arises as each state is formed by excitations from HOMO to successive higher-energy unoccupied orbitals. Specifically, S_1 involves excitation to LUMO, S_2 to LUMO+1, S_3 to LUMO+2, and S_4 to LUMO+3. Additionally, these unoccupied orbitals predominantly receive contributions from various aromatic fragments within the molecule (Fig. 5 and Table 4). Therefore, we can observe that the absence of transitions of LC nature in compound **1** causes the excited states of this compound to have a greater MLCT character than those of compound **3**. This enhances the 'heavy atom effect' in **1**, which is expected to amplify its spin orbit coupling (SOC) and intersystem crossing (ISC) rates.

The excitation energies for the T_1 and T_2 states of **3**, at 1.50 eV, are notably low. These energies primarily arise from electron excitations moving from HOMO−1 and HOMO−2 to LUMO and LUMO+1, which are mainly centred on the benzo-quinoxaline moiety as mentioned above (Fig. 5 and Table 4). Aromatic ligands can better delocalize the unpaired electrons in the triplet state, resulting in greater stabilization of the

Table 4 Vertical excitation energies (eV) of S_1–S_4, T_1–T_4 states and percentages (values in brackets) of dominant contributions to the calculated transitions for **1** and **3** obtained at the TD-DFT (SMD, acetonitrile)/6-31G(d,p)//SDD level

	Energy/eV		Electronic structure	
State	**1**	**3**	**1**	**3**
S_1	2.61	2.38	$d/\pi_H \rightarrow \pi^*_L$ (98) (MLCT/LLCT)	$d/\pi_H \rightarrow \pi^*_L$ (95), $\pi_{H-2} \rightarrow \pi^*_L$ (4) (MLCT/LC)
S_2	2.67	2.42	$d/\pi_H \rightarrow \pi^*_{L+1}$ (98) (MLCT/LLCT)	$d/\pi_H \rightarrow \pi^*_{L+1}$ (48), $\pi_{H-1} \rightarrow \pi^*_L$ (35), $\pi_{H-2} \rightarrow \pi^*_{L+1}$ (16) (MLCT/LC)
S_3	2.74	2.43	$d/\pi_H \rightarrow \pi^*_{L+2}$ (97) (MLCT/LLCT)	$\pi_{H-2} \rightarrow \pi^*_L$ (58), $\pi_{H-1} \rightarrow \pi^*_{L+1}$ (39) (LC)
S_4	3.06	2.45	$d/\pi_H \rightarrow \pi^*_{L+3}$ (94) (MLCT/LLCT)	$d/\pi_H \rightarrow \pi^*_{L+1}$ (48), $\pi_{H-2} \rightarrow \pi^*_{L+1}$ (27), $\pi_{H-1} \rightarrow \pi^*_L$ (23) (MLCT/LC)
T_1	2.31	1.50	$\pi/d_{H-3} \rightarrow \pi^*_L$ (23), $d_{H-4} \rightarrow \pi_{L+1}$ (19), $\pi/d_{H-2} \rightarrow \pi_{L+1}$ (17), $d_{H-5} \rightarrow \pi_L$ (13) (MLCT/LLCT)	$\pi_{H-1} \rightarrow \pi^*_L$ (48), $\pi_{H-2} \rightarrow \pi^*_{L+1}$ (44) (LC)
T_2	2.45	1.50	$\pi/d_{H-3} \rightarrow \pi^*_{L+1}$ (21), $d_{H-4} \rightarrow \pi_L$ (20), $\pi/d_{H-2} \rightarrow \pi_L$ (20), $d_{H-5} \rightarrow \pi_{L+1}$ (13) (MLCT/LLCT)	$\pi_{H-2} \rightarrow \pi^*_L$ (46), $\pi_{H-1} \rightarrow \pi^*_{L+1}$ (46) (LC)
T_3	2.41	2.22	$d_H \rightarrow \pi^*_{L+1}$ (73), $\pi_{H-1} \rightarrow \pi^*_L$ (13), $\pi_{H-7} \rightarrow \pi^*_L$ (4) (MLCT/LLCT)	$d/\pi_H \rightarrow \pi^*_L$ (66), $\pi_{H-3} \rightarrow \pi^*_{L+1}$ (10) (MLCT/LLCT)
T_4	2.48	2.26	$d_H \rightarrow \pi^*_L$ (79), $\pi_{H-1} \rightarrow \pi^*_{L+1}$ (9), $\pi/d_{H-3} \rightarrow \pi^*_L$ (4) (MLCT/LLCT)	$d/\pi_H \rightarrow \pi^*_{L+1}$ (77), $\pi_{H-3} \rightarrow \pi^*_L$ (14) (MLCT/LLCT)

excited state. This stabilization leads to the small excitation energy observed in these states with a ^{3}LC/$^3\pi\pi^*$ nature. Regarding T_3 and T_4, they showed a MLCT/LLCT character which involves transitions from HOMO and HOMO−3 to LUMO and LUMO+1, which implicates charge transfers from the metal, fused benzene and pyridine moieties to the benzoquinoxaline fragment. These states are much closer in energy to S_1 (^{1}MLCT/^{1}dπ^*) and S_2 (^{1}LC/$^1\pi\pi^*$) states than T_1 and T_2 states (^{3}LC/$^3\pi\pi^*$). Regarding **1**, the excitation energies for T_1–T_4 states are closely matched, exhibiting MLCT/LLCT characteristics. These states exhibit a substantial multiconfigurational nature due to excitations across multiple orbitals. This contrasts with the singlet excited states, which only involve single excitations (Table 4).

The strength of SOC is influenced by the energy gap between adiabatic excitation energies, which encompass the coupling between electronic and nuclear motions. Therefore, we calculated these adiabatic excitation energies in electron volts (eV) for the optimized excited states (Fig. 6 and Table S8†). For compound **3**, the substantial energy gap between the S_1 and T_1/T_2 states (1.56 eV) significantly restricts intersystem crossing (ISC) between these states, consistent with the Fermi golden rule.[120] Moreover, the almost complete absence of d orbitals in the metal configurations of the T_1/T_2 states due to their $^3\pi\pi^*$ character contributes to weaker SOC, further inhibiting ISC between these states. In contrast, the smaller energy gaps between the S_1 and T_3/T_4 states (0.160 eV and 0.07 eV, respectively) are expected to promote ISC. Additionally, the adiabatic excitation energies of the T_3 and T_4 states (2.074 eV and 2.160 eV, respectively) are relatively close to the vertical excitation energies of the T_1 and T_2 states (1.50 eV). This proximity suggests potential overlap of vibrational levels, which could facilitate internal conversion (IC) as a relaxation pathway from higher triplet states through vibronic coupling mechanisms. The small energy gap observed between the adiabatic energies of S_0 and T_1/T_2 states (0.69 eV) suggests a non-emissive character for these states, along with a long-lived nature due to their $\pi\pi^*$ configuration.

The triplet–triplet energy transfer process is efficient when the triplet state energy exceeds the energy required to excite molecular $^3O_2$ to $^1O_2$ (approximately 0.98 eV or 1270 nm). Although this calculated energy gap is below the threshold required for direct $^1O_2$ generation, it is important to consider that TD-DFT methodology is well known to underestimate the energy of $\pi\pi^*$ singlet and triplet excitations states, which suggests the energy for T_1/T_2 state is likely too low.[121,122] Indeed, several studies have found systematic "red-shifts" in TD-DFT/B3LYP predicted triplet energies for states both large aromatic chromophores and organometallic complexes.[123,124] Consequently, the actual adiabatic T_1/T_2 energy in our system, which is not far from 0.98 eV, is plausibly higher than the TD-DFT result, likely in the range necessary to achieve $^1O_2$ sensitization. This alignment with the observed $^1O_2$ generation supports the photophysical conclusions of this study. Additionally, the long lifetime of this state may favour direct electron transfer from the triplet state to molecular oxygen, leading to the formation of $O_2^{\bullet-}$, either through direct interaction or *via* an intermediate electron donor or substrate.[125]

In compound **1**, similar energy gaps were observed between the S_1 and T_3/T_4 states, specifically 0.178 eV and 0.082 eV, respectively, as compared with **3**. The absence of isoenergetic π orbitals (HOMO−1 and HOMO−2) relative to the HOMO increases the involvement of metal-centred orbitals in the transitions of these singlet excited states. Consequently, as stated, spin–orbit coupling (SOC) is expected to be more effective in **1** than in **3**. Additionally, differences in the orbital geometries involved in these singlet and triplet excited states (see Table 4) further enhance SOC, in accordance with El Sayed's rule.[126]

Moreover, a key difference observed in **1** compared with **3** is the significantly smaller energy gaps between the S_1 and T_1/T_2 states (approximately 0.414 eV). These observations suggest the presence of two possible competing ISC channels. The first is a thermally activated ISC between S_1 and T_2/T_3 states. Due to the very small energy gaps and the different orbital geometries, the SOC will be very efficient, leading to rapid ISC. IC from T_2/T_3 to T_1/T_2 is also fast, quickly populating the lowest excited

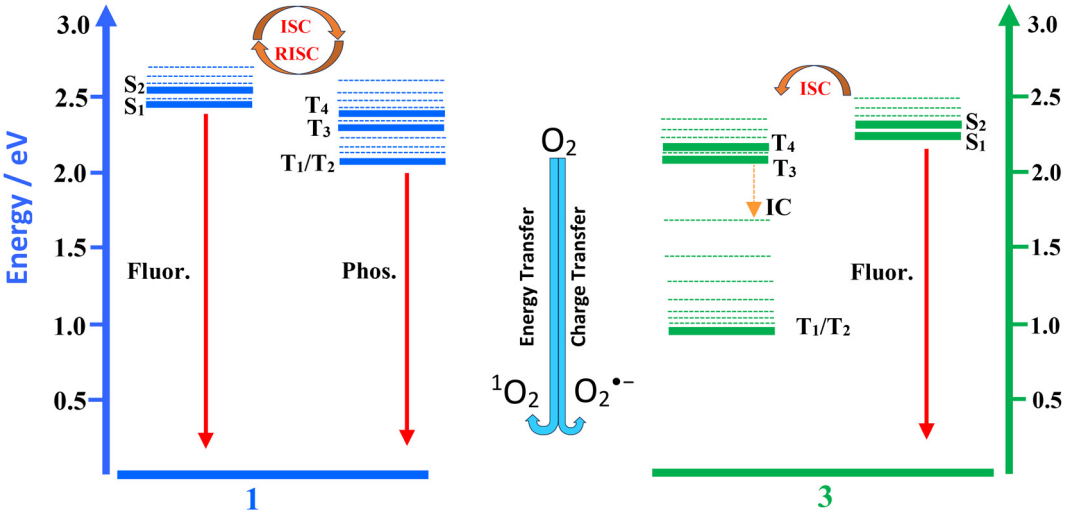

Fig. 6 Proposed Jablonski diagram for **1** and **3** and their interaction with molecular oxygen. Triplet excited states can undergo electron transfer generating $O_2^{\bullet-}$ or energy transfer to molecular oxygen producing $^1O_2$.

triplet states. The second channel is a slow ISC between S_1 and T_1/T_2, as the orbitals of S_1 and T_1/T_2 are almost identical, reducing the SOC rate, and the energy gap between them is significantly larger. Furthermore, the small energy gaps between T_1 and T_4 states cause the vibrational levels of the higher triplet states to overlap with those of the lower triplet states, facilitating vibronic coupling and enabling reverse internal conversion (IC).[127] This overlap increases the probability of rapid electron exchange among the T_1–T_4 states, allowing for a large number of electron configurations and enhancing the return to the singlet manifold *via* reverse intersystem crossing (RISC).[128] Therefore, the expected larger SOC of **1**, due to the greater MLCT character of the S_1 state and the multiconfigurational character of the T_1–T_4 states, as well as the existence of several channels to produce ISC in this compound, suggests the existence of a more efficient population of triplet states where the electron can undergo rapid exchange between these states due to their close energy levels. This spreads the population over various triplet states, prolonging the overall triplet-state lifetime. The longer lifetime of the triplet states in **1**, compared with **3**, should contribute to an enhanced production of ROS from the former compound. Further experiments on the emission profile of **1** in acetonitrile were also performed, both at room temperature and at 77 K. These spectra allowed us to effectively determine the energy gap through the difference of the energy of the *onset* from the emission bands at RT and 77 K (Fig. S80†). These results are consistent with TD-DFT calculations, as well as the observed delayed fluorescence and the higher values obtained in the case of **1** for the quantum yields of emission and ROS generation.

2.6 Biological studies

Anticancer activity. The phototoxic activity of complexes **1** and **3** against different cancer cells was first evaluated using MTT (3-[4,5-dimethylthiazol-2-yl]-2,5 diphenyl tetrazolium bromide) assays under dark and light conditions. Under the experimental conditions, light exposure was confirmed to exert a minimal effect on cell viability. However, to ensure accurate assessment of cytotoxicity, the viability of cells subjected to light or dark treatments was analyzed relative to untreated control cells that were exposed to the same irradiation conditions as the treated cells. As summarized in Table 5, after 48 h of treatment in the dark, both complexes exhibited intrinsic cytotoxicity, with $IC_{50,dark}$ values ranging from 0.89 to 3.65 μM. These values were comparable to that of the chemotherapeutic agent cisplatin. In all cases, complex **1** displayed moderately higher cytotoxicity than complex **3**. Notably, upon photoactivation with blue light (460 nm, 24.1 J cm^{-2}), the activity of both complexes significantly increased, resulting in $IC_{50,light}$ values in the nanomolar range and phototoxic indexes (PIs) between 11 and 32 for complex **1** and from 6 to 124 for complex **3**. Again, complex **1** exhibited higher photocytotoxicity than complex **3**, except in A549 lung cancer cells, where complex **3** displayed an outstanding photodynamic activity, resulting in a PI of 124 and an $IC_{50,light}$ of 0.016 μM. Given the favorable photodynamic behavior of the complexes, their photocytotoxic activity was also examined in A549 cells after activation with green (515 nm) and red (635 nm) light, which possess deeper tissue penetration properties.[129] Following green light irradiation, $IC_{50,light}$ values of 0.18 ± 0.03 μM were obtained for complex **1** and 0.204 ± 0.01 μM for complex **3**, representing PI values of 5 and 11. However, irradiation with red light only produced a 2-fold increase in the cytotoxicity of complex **1** and a 4-fold increase in the cytotoxicity of complex **3** compared with treatments in dark conditions, respectively, with $IC_{50,light}$ values of 0.49 ± 0.1 μM and 0.502 ± 0.04 μM. These results confirm that optimal photoactivation for both complexes is achieved with blue light irradiation, which agrees with their absorption spectra. However, green light could also induce a significant phototoxic

Table 5 Photocytotoxic activity of the complexes in 2D cell cultures

	1			3			Cisplatin
	IC_{50} (μM)		PI	IC_{50} (μM)		PI	IC_{50} (μM)
Complex	Dark	Light		Dark	Light		Dark
A549	0.890 ± 0.204	0.028 ± 0.019	32	2.028 ± 0.784	0.016 ± 0.003	124	5.998 ± 1.185
HeLa	1.048 ± 0.253	0.063 ± 0.014	17	2.515 ± 0.173	0.252 ± 0.059	10	1.528 ± 0.326
MCF-7	1.142 ± 0.164	0.100 ± 0.024	11	3.310 ± 0.093	0.535 ± 0.059	6	5.750 ± 0.070
BxPC3	0.984 ± 0.062	0.078 ± 0.018	13	3.652 ± 0.261	0.140 ± 0.055	26	1.008 ± 0.009
MRC-5	2.587 ± 0.199	0.125 ± 0.032	21	3.067 ± 0.409	0.292 ± 0.008	10	5.327 ± 0.377

Cells were treated with the compounds for 4 h at 37 °C to ensure their maximum internalization and then kept in the dark or irradiated with blue light for 1 h (460 nm, 24.1 J cm^{-2}). Cell viability was assessed 43 h later by MTT assays. Data represent the mean ± SD of at least three independent experiments, each performed in triplicate. PI: phototoxicity index = $IC_{50,dark}/IC_{50,light}$.

response. These results can be compared with those obtained with analogous Ir complexes with bpy and C^N ligands with less π-extension using MCF-7 breast cancer cells. With ppy, there was no increase in cytotoxicity by light activation.[108] With C^N ligands with moderate π-expansion as 2-phenylquinolinate (2pq), and 1-phenylisoquinolinate (1pq), the obtained PI values (up to 5.9) were lower and the $IC_{50,light}$ values (0.83 or 0.63 μM) were 8 or 6 times higher than those obtained with our compounds, reflecting the beneficial effect of the π-expansion of our ligands.[108]

It should be noted that, in general, the complexes exerted comparable cytotoxicity against the cancer cell lines and non-malignant MRC-5 fibroblasts in dark conditions, revealing a lack of intrinsic selectivity towards malignant cells. However, a remarkable photoselectivity was observed when comparing the effects of the photoactivated complexes on A549 lung cancer cells to the dark toxicity against MRC-5 lung fibroblasts. Upon irradiation, the $IC_{50,light}$ values of complexes **1** and **3** in A549 cells were 92.4 and 191.7 times lower, respectively, than the $IC_{50,dark}$ values determined in MRC-5 cells. These findings show the potential of these complexes to exert a selective light-activated action against cancer cells with minimal effects on the non-irradiated healthy tissue.

To further assess the toxicity of the complexes, hemolytic experiments were conducted.[130] Porcine red blood cells (RBC) were incubated with **1** and **3** in the dark or under blue light irradiation at concentrations close to the $IC_{50,dark}$ (1 μM) or $IC_{50,light}$ (0.2 μM and 0.02 μM). Hemoglobin release was measured as an indicator of the capacity of the complexes to destabilize RBC membranes. Both complexes exhibited minimal hemolytic activity (≤5% hemolysis) under these conditions, indicating a favorable compatibility with blood cells in the context of potential intravenous administration (Table S9†).

The anticancer activity of **1** and **3** was further evaluated using clonogenic assays, which better assess the long-term survival and proliferative potential of cells following the treatment.[131] HeLa cells were selected for this study due to their superior ability to form colonies *in vitro*. Cells were exposed to complexes **1** and **3** at the respective $IC_{50,light}$ values for 4 h, followed by incubation in dark conditions or under blue light irradiation. Ten days later, the number of colonies formed in the absence of light irradiation was similar to that of the corresponding untreated control, indicating the absence of a cytotoxic effect. In contrast, photoactivation of the complexes significantly reduced colony numbers to 41.0 ± 4.9% for complex **1** and 52.2 ± 2.9% for complex **3** (Fig. 7). No significant differences were observed between dark and light conditions for both untreated cells and cells treated with cisplatin, consistent with the non-photoactivatable nature of cisplatin. These results support the light-dependent anticancer activity of the complexes at the $IC_{50,light}$ values determined in MTT assays. Furthermore, they demonstrated the capability of the complexes to inhibit the clonogenic potential of the cells, a critical factor in preventing metastasis, as proliferation in distant tissues is essential for the formation of secondary tumors.

Intracellular ROS generation. To elucidate the mechanism underlying the photocytotoxicity of the complexes, their capacity to generate ROS at the cellular level was investigated. This is a primary characteristic for PSs to be effective in photodynamic therapy (PDT). The cellular ROS levels were quantified using the dichlorodihydrofluorescein diacetate (H2DCFDA) probe, which is converted to the green fluorescent derivative dichlorofluorescein (DCF) upon oxidation. A549 and HeLa cells were treated with **1** and **3** at their respective $IC_{50,light}$ and changes in cellular fluorescence were monitored by flow cytometry. As shown in Fig. 8A, no significant differences in cell fluorescence were observed in the absence of light irradiation compared with untreated control cells. However, blue light irradiation induced a marked increase in the green fluorescent signal, indicating ROS generation within the cells. Specifically, treatment with complex **1** resulted in a 10.4 ± 0.7-fold increase in fluorescence intensity in A549 cells and an 8.51 ± 2.8-fold increase in HeLa cells. Complex **3** also induced a strong fluorescence rise, with a 14.61 ± 0.9-fold increase in A549 cells and a 16.95 ± 3.5-fold increase in HeLa cells. As was demonstrated, these complexes were able to generate singlet oxygen under light irradiation (Fig. S56 and S57†). This type II reaction is the primary cytotoxic mechanism for most PSs in PDT.[132] Furthermore, by the DHR123 test, it was shown that the complexes showed the ability to produce superoxide anions ($O_2^{\bullet-}$)

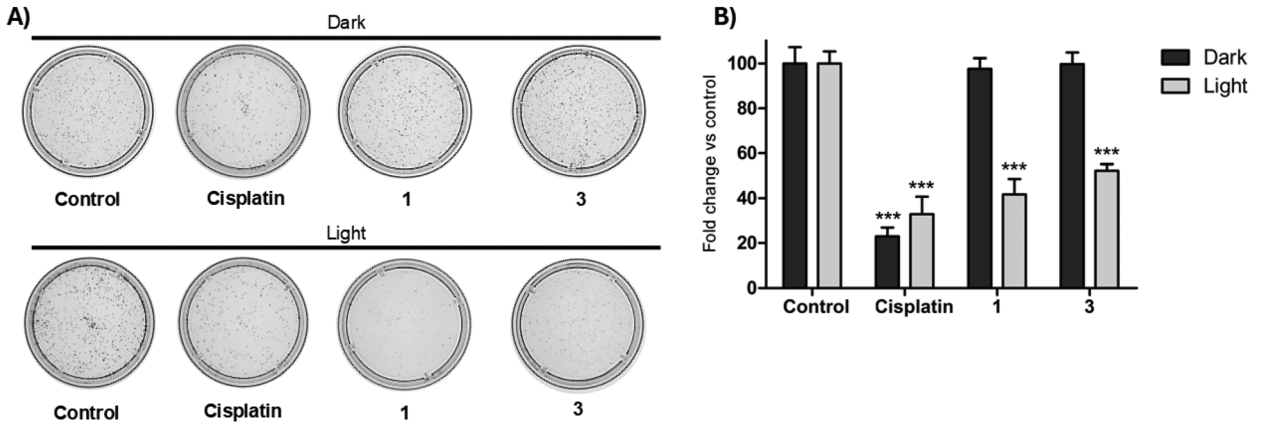

Fig. 7 Clonogenic assays. (A) Images of the colonies generated after exposure of HeLa cells to complexes **1** and **3** at the corresponding $IC_{50,light}$, or medium alone as a control, both in the dark or with blue light irradiation (1 h, 460 nm, 24.1 J cm^{-2}). Cisplatin at 5 μM was used as the positive control. (B) Bar charts represent the percentage of colonies after each treatment relative to the control cells (mean ± SD of three experiments). *** $p < 0.001$.

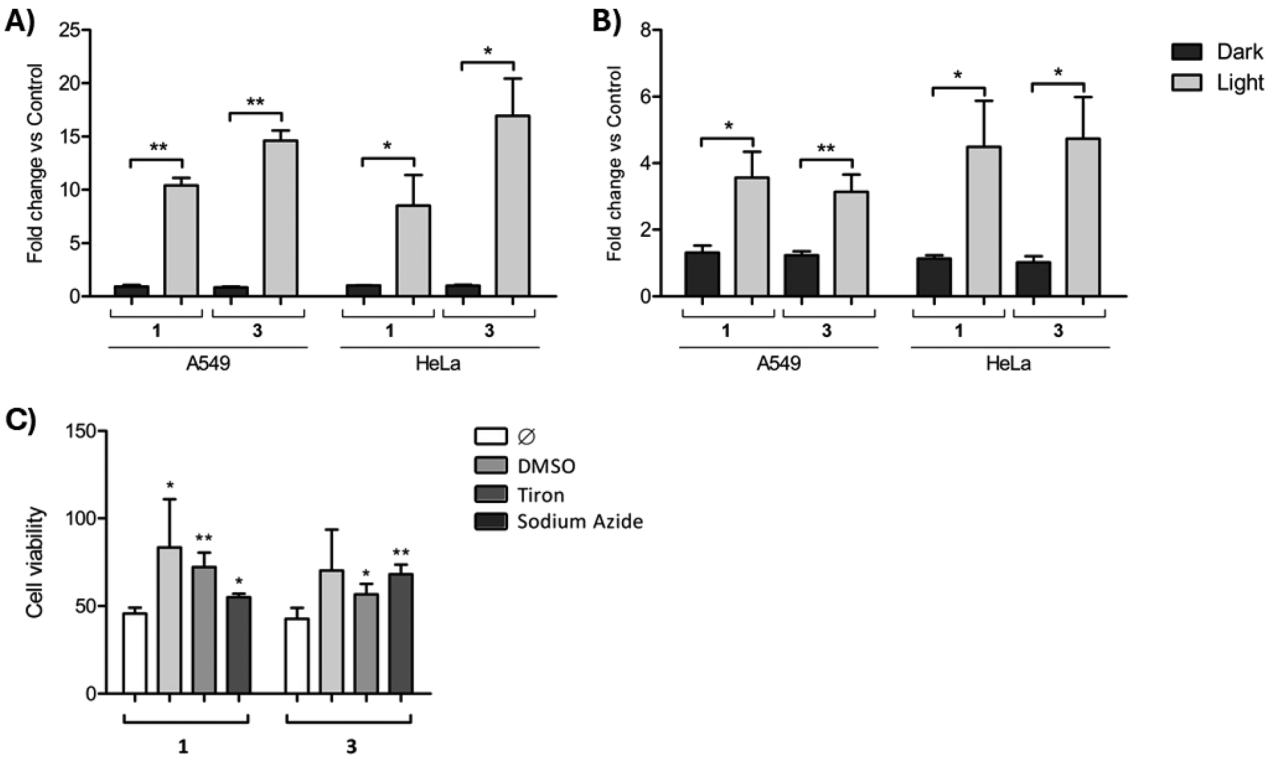

Fig. 8 Intracellular ROS generation and effect of specific ROS on cell viability. A549 and HeLa cells were treated with complexes **1** and **3** at their respective $IC_{50,light}$ for 4 h, followed by incubation in the dark or exposure to blue light irradiation for 1 h (460 nm, 24.1 J cm^{-2}). The elevation of general ROS (A) and superoxide anion (B) levels were determined with specific probes and cell fluorescence was measured by flow cytometry. Bars represent the mean fold increase (±standard deviation) relative to untreated control cells from three independent experiments. *$p < 0.05$; **$p < 0.01$ *versus* non-irradiated cells. (C) HeLa cells were treated at their $IC_{50,light}$ and exposed to blue light irradiation either without (∅) or with specific ROS scavengers (DMSO for $^{\bullet}OH$, sodium azide for $^1O_2$, or tiron for $O_2^{\bullet-}$). Bars indicate the mean percentage of viable cells (±standard deviation) 48 hours post-treatment relative to untreated control cells incubated with medium alone or with the corresponding scavenger. * $p < 0.05$; ** $p < 0.01$ compared with treated cells without scavengers. Each condition was tested in triplicate across three independent experiments.

(Fig. S62†) and, thus, undergo type I PDT processes. $O_2^{\bullet-}$ is a transient but highly reactive species that originates oxidative cascades, causing substantial and potentially irreversible damage to cellular components.[133] Consequently, the contribution of this radical to the photocytotoxic activity of the complexes was investigated. Generation of $O_2^{\bullet-}$ was quantified using the Superoxide Detection Reagent (Enzo Life Sciences), which emits an orange signal upon interaction with this

radical. As expected, no significant differences in fluorescence emission were observed when treatments were conducted in dark conditions compared with control cells. Conversely, treatment with photoactivated complex **1** resulted in a 3.57 ± 0.78-fold and 4.49 ± 1.38-fold increase in fluorescence emission in A549 and HeLa cells, respectively. Similarly, complex **3** induced a 3.14 ± 0.52-fold and 4.73 ± 1.26-fold increase in fluorescence in A549 and HeLa cells (Fig. 8B), confirming $O_2^{\bullet-}$ generation within cells, with a similar activity for both complexes. It should be noted that these results differed from those previously obtained with the DHR123 test, where a higher superoxide anion production was observed for complex **1**. This discrepancy may be attributed to the detection of endogenous mitochondrial superoxide radicals. Mitochondrial electron transport chain (ETC) leakage is a well-established source of superoxide radicals.[134] Thus, the activity of complexes **1** and **3** in mitochondria could potentially disrupt ECT which may result in further intrinsic $O_2^{\bullet-}$ generation. Finally, it should be noted that no clear correlation was observed between the ROS levels and the PI of complexes **1** and **3** in A549 and HeLa cells, which suggests that additional factors may contribute to the photocytotoxic activity of these complexes.

Finally, to validate the contribution of individual ROS to the photocytotoxic activity of the complexes, HeLa cells were incubated with complexes **1** and **3** at their respective $IC_{50,light}$ and irradiated with blue light in the presence of specific ROS scavengers (dimethyl sulfoxide (DMSO) for $^{\bullet}OH$, sodium azide for $^1O_2$ or tiron for $O_2^{\bullet-}$) or with medium alone as a control. Cell viability was determined 48 h post-treatment. As shown in Fig. 8C, the percentage of viable cells significantly increased when treatments were conducted in the presence of sodium azide and tiron, confirming the involvement of $^1O_2$ and $O_2^{\bullet-}$ in the photocytotoxic mechanism of both complexes. Furthermore, the cytotoxic effect of complex **1** was also inhibited by DMSO, suggesting a contribution from $^{\bullet}OH$.

These results collectively demonstrate that type II photochemical processes play a predominant role in the photocytotoxicity of these complexes. Furthermore, the involvement of $O_2^{\bullet-}$ and $^{\bullet}OH$ supports the contribution of type I mechanisms, which exhibit reduced dependence on molecular oxygen. Thus, these complexes hold potential for treating cancer cells in hypoxic microenvironment, where resistance to conventional photodynamic therapy is often observed.

Mitochondrial damage. Cationic iridium-based complexes bearing lipophilic ligands have a high propensity to accumulate in the mitochondria, driven by the negative potential across the inner mitochondrial membrane. The lipophilicity of our complexes was quantified by determining their octanol/water partition coefficients ($\log P_{o/w}$) using the traditional shake-flask method. Complexes **1** and **3** displayed $\log P_{o/w}$ values of 1.15 ± 0.27 and 1.58 ± 0.23, respectively, indicating their lipophilic character and a high probability of mitochondrial localization.[52] This cellular distribution is particularly significant because mitochondria are involved in essential cellular functions, including the production of adenosine triphosphate (ATP), the regulation of apoptosis, and the maintenance of the redox homeostasis. The disruption of these processes ultimately results in cell death, thereby establishing mitochondria as a primary therapeutic target in cancer. As described below (Fig. 14), confocal microscopy experiments with complex **1** confirmed a high degree of co-localization of the complex with mitochondria.

Thus, the effect of the complexes on mitochondrial function was investigated as a potential cytotoxic mechanism. HeLa cells were treated with complexes **1** and **3** under dark and light conditions and mitochondrial integrity was assessed by confocal microscopy using the fluorescent dye MitoTracker™ Red CMXRos, which accumulates within healthy mitochondria based on the mitochondrial membrane potential (MMP).[135] As shown in Fig. 9A, intense red mitochondrial staining was detected in both control cells and cells treated in the dark. However, upon photoactivation, the staining was significantly attenuated, revealing mitochondrial damage. To corroborate these results, changes in the MMP were assessed using the JC-1 dye, which emits red fluorescence when accumulated in healthy mitochondria and green fluorescence when the MMP is dissipated. As shown in Fig. 9B, 94.49% of untreated control cells exhibited red fluorescence emission from JC-1. This percentage was similar for cells treated with complexes **1** (91.64%) and **3** (88.42%) in the dark, while it decreased to 44.04% for complex **1** and 43.16% for complex **3** upon blue light irradiation. Overall, these results corroborated the activity of the complexes at the mitochondrial level.

Photocatalytic oxidation of NADH. Nicotinamide adenine dinucleotide (NAD) is a crucial coenzyme in cellular metabolism that acts as an electron carrier in redox reactions.[136] NADH, which is the reduced form of NAD, transfers electrons to the mitochondrial ETC to generate ATP. This crucial role in the cell energy generation has made NADH a promising target in anticancer therapy.[107,137–141] The oxidation of NADH by anticancer agents disrupts ATP generation and contributes to mitochondrial dysfunction. In recent years, several papers have been published on the photocatalytic oxidation of NADH by Ir(III) complexes *via* a single-electron transfer (SET) mechanism with generation of $O_2^{\bullet-}$ and carbon-center radicals.[107,137] This suggests an additional potential mechanism of action for Ir(III) complexes in type I PDT, which we have investigated for our complexes.

The evolution of NADH in the presence of complexes **1** and **3** (complex/NADH ratio = 1/100) was monitored by UV–vis spectroscopy in aqueous solution over a period of 10 minutes at room temperature. In order to evaluate the light effect in the oxidation reaction, the experiment was carried out in dark conditions and upon blue light irradiation (470 nm, 51.4 mW cm^{-2}). The evolution of the photocatalytic reaction was monitored by the decrease of the absorption band at 340 nm (Fig. S81–S83†). In dark conditions, a very low level of NADH oxidation was observed. However, the reaction under light irradiation was very fast for both complexes. The reaction pro-

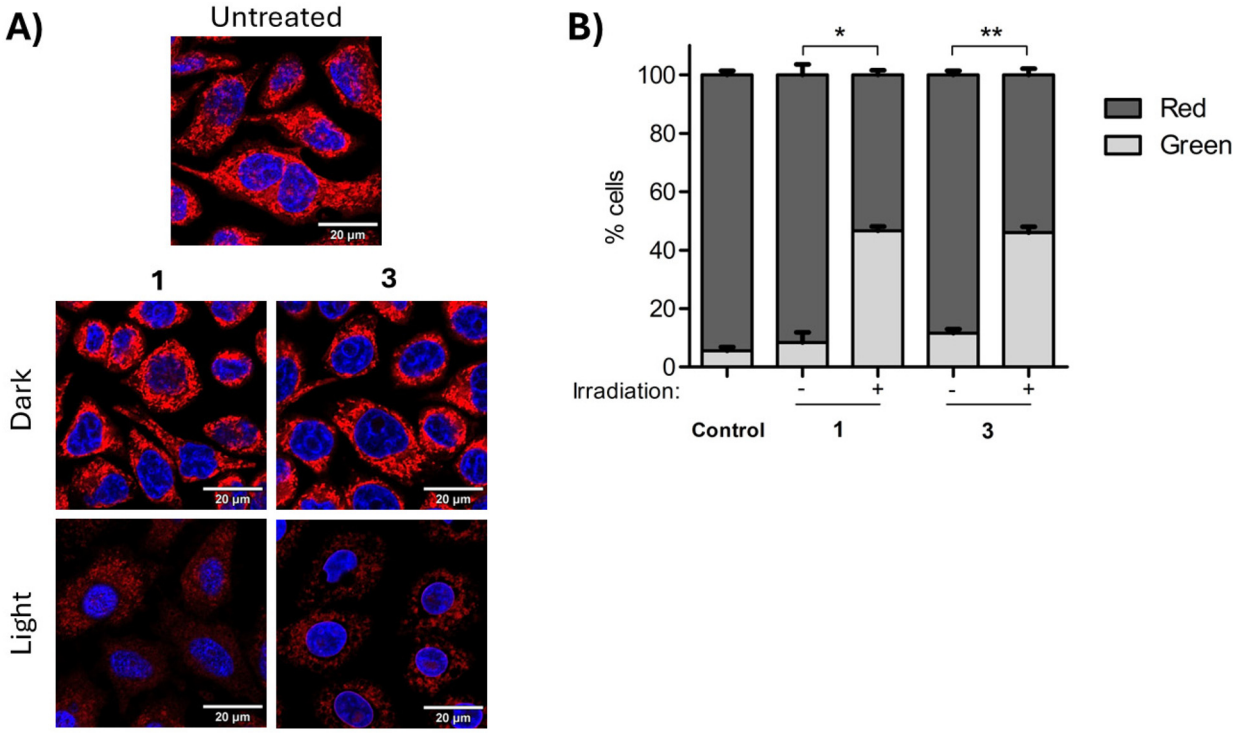

Fig. 9 Effect on mitochondria. HeLa cells were incubated with complexes **1** and **3** at the corresponding $IC_{50,light}$ for 4 h at 37 °C and then kept in darkness or exposed to blue light for 1 h. (A) Confocal microscopy images of the cells. Cell nuclei were localized in blue with Hoescht (λ_{ex}: 400 nm; λ_{em}: 450 nm), and healthy mitochondria were labelled with MitoTracker™ Red CMXRos (λ_{ex}: 543 nm; λ_{em}: 595 nm). Attenuation of red fluorescence emission upon irradiation indicates mitochondrial dysfunction. (B) Percentage of cells exhibiting green and red JC-1 fluorescence after treatment in dark or irradiated conditions (mean ± SD of three independent experiments). Cells incubated with medium alone were used as control. Loss of MMP was determined by a decrease in the percentage of red fluorescent cells. * $p < 0.05$; ** $p < 0.01$.

ceeded with first-order kinetics with respect to NADH. The TONs (Turnover Numbers, measured after 5 minutes) of the complexes were up to 46 (Fig. S83 and Table S10†) and TOFs (Turnover Frequencies) were up to 555 h^{-1}, which make complexes **1** and **3** among the most active NADH photocatalysts.[107,138] As has been reported for other Ir(III) photosensitizers, H_2O_2 was detected (test strips) in the photocatalytic NADH oxidation with **1** and **3**,[107] which indicates the generation of $O_2^{\bullet-}$ and the conversion to H_2O_2.

Cell death mechanism. The depolarization of the mitochondrial membrane is a critical event that can initiate programmed cell death *via* apoptosis. To assess the apoptotic potential of complexes **1** and **3**, flow cytometry experiments were conducted using annexin V-FITC and propidium iodide (PrI) staining. Viable cells are impermeable to both dyes, whereas early and late apoptotic cells exhibit annexin V binding due to phosphatidylserine exposure on the cell surface. In addition, late-apoptotic and necrotic cells are PrI-positive, due to the loss of membrane integrity. Treatments with cisplatin were included as a positive control for apoptosis. As shown in Fig. 10, treatments with photoactivated complexes **1** and **3** at the corresponding $IC_{50,light}$ led to a significant increase in both the early and late apoptotic populations to 10.98 ± 2.03% and 6.26 ± 3.01%, respectively, for complex **1**, and to 17.64 ± 10.48% and 6.63 ± 4.66% for complex **3**. Treatments using five times the $IC_{50,light}$ resulted in higher apoptotic rates, with early and late apoptotic populations, respectively, reaching 21.46 ± 15.31% and 35.78 ± 15.37%, for complex **1** and 21.48 ± 15.55% and 28.91 ± 20.54% for complex **3**. Importantly, minimal necrotic cell populations were observed across all treatment conditions. These findings indicate that the complexes induce a form of programmed cell death involving apoptosis, thereby minimizing potential collateral tissue damage and inflammatory responses typically associated with necrosis.[142]

However, the lower apoptotic population induced by complex **1** in comparison with the cisplatin control (Fig. 10) suggests that apoptosis may not be the exclusive primary death mechanism. Concurrent with this observation, the rapid photocatalytic oxidation of NADH induced by complex **1**, coupled with the significant increase in cellular reactive oxygen species (ROS) levels and mitochondria shrinkage, suggest the involvement of ferroptosis. Ferroptosis is a distinct form of regulated cell death characterized by iron-dependent lipid peroxidation and is intrinsically linked to oxidative stress. Recent literature demonstrates the capacity of various metal-based complexes, including iridium(III) complexes, to induce ferroptosis or other non-apoptotic pathways, such as pyroptosis.[143–145] Therefore, while apoptosis remains a key cell death mechanism, other non-apoptotic pathways, potentially

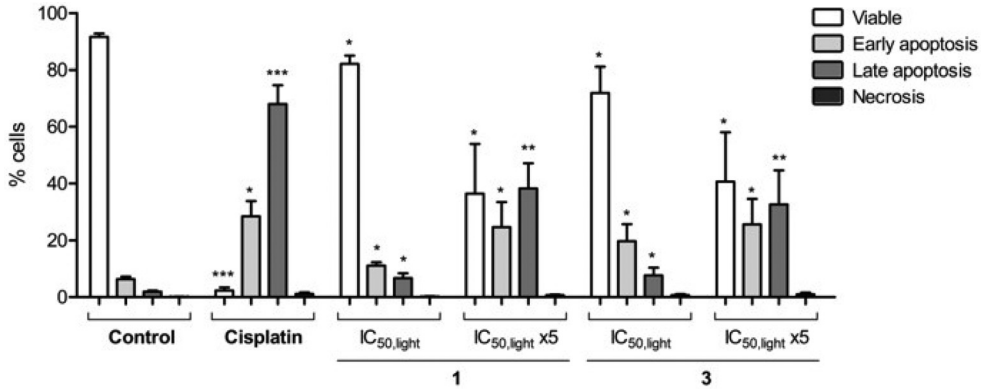

Fig. 10 Cell death mechanism. HeLa cells were treated with complexes **1** and **3** for 4 h at the $IC_{50,light}$ or five times $IC_{50,light}$. Cisplatin (5 μM) was used as positive control. Cells were double stained with propidium iodide and Annexin V-FITC. Bars represent the percentages of viable, early apoptotic, late apoptotic, and necrotic cells after each treatment (mean ± SD) determined in three independent experiments. Statistical analysis was performed compared with untreated cells. * $p < 0.05$; ** $p < 0.01$; *** $p < 0.001$.

including ferroptosis, may also contribute to the overall toxicity of complex **1**.

Cell migration. Mitochondrial energy production is crucial for modifying focal adhesions and cytoskeleton remodeling, which are essential processes for cell migration.[146] The migratory capacity is of particular relevance in the context of cancer, as it enables the invasion of surrounding tissues, which represents the initial step of the metastatic cascade that ultimately enables cancer cell dissemination from the primary tumor to distant organs.[147] Given the mitochondrial-targeted activity of complexes **1** and **3**, their impact on cell migration was evaluated using wound healing assays. In the absence of light, A549 cells treated with complexes **1** and **3** at the $IC_{50,light}$ demonstrated effective scratch closure in the cell monolayer, with migration rates comparable to the control cells (Fig. 11). However, following photoactivation, a significant reduction in the wound closure was observed, with an 88.4% inhibition in the cell migration rate for complex **1** and a 93.0% inhibition for complex **3**, compared with control cells. In contrast, cisplatin treatment resulted in only a moderate reduction in cell migration. This substantial difference suggests that complexes **1** and **3** exhibit additional characteristics in their antitumor action that could potentially be exploited for the prevention of metastasis.

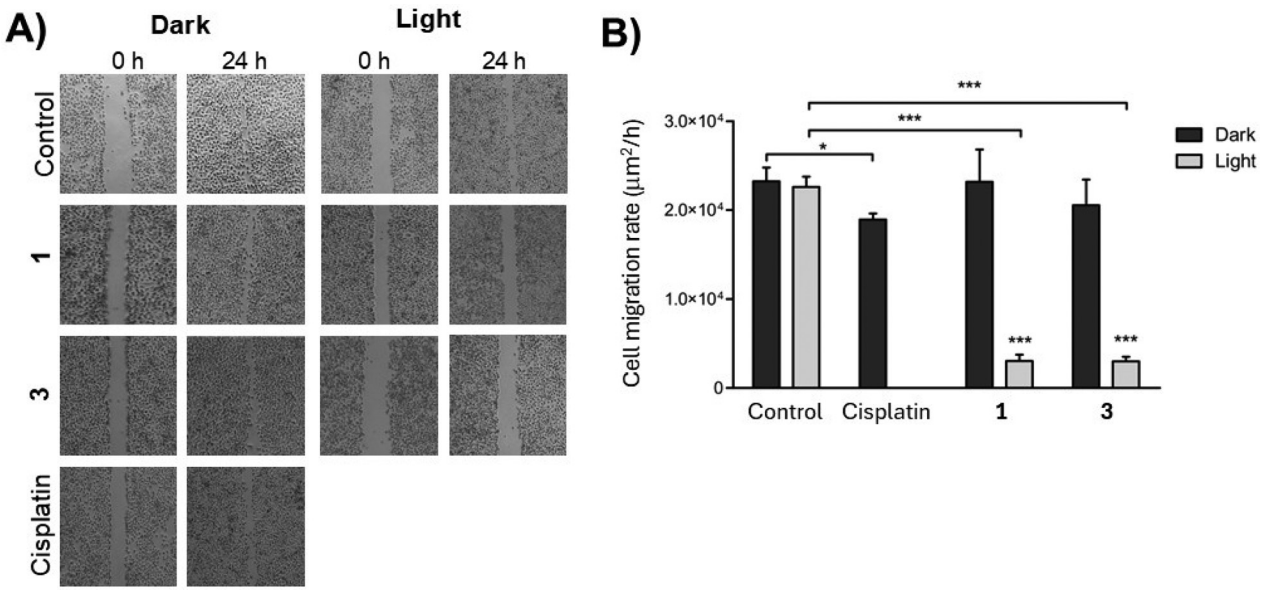

Fig. 11 Wound healing assays. A549 cells were incubated with complexes **1** and **3** at their respective $IC_{50,light}$, either in the dark or under blue light irradiation. Cisplatin (5 μM) was used as a control. (A) Representative images of the wound at time 0 and its closure after 24 h. (B) Migration rate ($\mu m^2 h^{-1}$) of cells exposed to the different treatments. Bars represent the mean ± SD of three independent experiments. * $p < 0.01$; *** $p < 0.001$ compared with the control or dark treatment.

Biological activity of NP1 and NP3. The encapsulation of compounds in nanoparticles (NPs) allows their selective accumulation in cancer cells, taking advantage of the EPR effect. In addition, NPs protect the complexes during their circulation in the blood system and improve their cellular uptake, especially if the non-encapsulated compounds tend to aggregate.[148] The influence of encapsulation on the photocytotoxic properties of the complexes was initially examined using two-dimensional (2D) monolayers of A549 and HeLa cells. Interestingly, compound **1** exhibited a marked increase in cytotoxicity when encapsulated in **NP1**. As shown in Table 6, the $IC_{50,dark}$ values of **NP1** in A549 and HeLa cells were, respectively, 14.6 and 15.2-fold lower than those of complex **1**. To rule out the possibility that this effect was due to the intrinsic cytotoxicity of the empty nanoparticle or the constituent polymers (**P1b** polymer with amine groups, and **P2**, polymer with carboxylic groups), their impact on cell viability was assessed under the same experimental conditions (Table S11†). No detectable toxicity was observed across a concentration range of up to 200 μg mL^{-1}, which exceeds the nanoparticle concentrations corresponding to the $IC_{50,dark}$ values of **NP1** and **NP3** in both cell lines.

Following blue light irradiation, the $IC_{50,light}$ values of **NP1** were further reduced, by 32.5-fold in A549 cells and 26.2-fold in HeLa cells compared with complex **1** (Table 6), yielding PI values of 70 and 28. These represent 2.2- and 1.6-fold increases over the PI values of complexes **1** obtained in A549 and HeLa cells, respectively. These results revealed that **NP1** exhibits excellent properties for PDT. Of particular relevance is the outstanding cytotoxic activity of **NP1** upon irradiation, evidenced by an $IC_{50,light}$ value of 0.86 nM in A549 cells. Compared with other iridium derivatives with IC_{50} < 10 nM (Table S12†), the activity of **NP1** is only surpassed by our recently described $[Cp^*Ir(C^N)L]^+$ derivatives with π-expansive ligands.[42] An identical IC_{50} value of 0.86 nM has been described for a complex of the type $[Ir(C^N)_2(NHC^NHC)]^+$, although ultraviolet irradiation was used.[149] Conversely, the dark activity of complex **3** was minimally affected by encapsulation. However, upon irradiation, the cytotoxicity of **NP3** was notably higher, leading to a remarkable increase in the PI value for **NP3** *versus* **3** (from 10 to 65) in HeLa cells. In contrast, in A549 cells the high PI value obtained for **3** decreased in **NP3** (from 124 to 45).

These results were validated using A549 multicellular spheroids (MCSs), which are 3D cell models that more closely reproduce tumor complexity and organization, including cell–cell interactions, nutrient distribution and oxygen gradients.[150,151] The IC_{50} values obtained indicated that MCSs were significantly less sensitive to both the free and encapsulated complexes than cells growing in monolayers (Table 6). The reduced efficacy in MCSs is consistent with observations for other chemotherapeutic agents, such as doxorubicin, and could be attributed to a population of quiescent cells within the spheroids that are less susceptible to the antiproliferative effects of the drugs.[152] Furthermore, the complex structure of MCSs has been described to hinder the diffusion of drugs and oxygen to the inner cell layers, further compromising the efficacy of the PSs. It is noteworthy that our complexes and NPs were able to exert a remarkable photocytotoxic effect against MCSs, resulting in a significant reduction in their size and a concomitant loss of refractivity, which is indicative of extensive cell death (Fig. 12A). Particularly, complex **1** and **NP1** exhibited a notable activity, with $IC_{50,light}$ values in the nanomolar range and PIs of 24.3 and 14.4, respectively (Table 6). As observed in the 2D cultures, the photocytotoxicity of **NP1** was found to be higher than that of the free complex **1**. The encapsulation of complex **3** also improved its photocytotoxic activity against MCSs. However, the $IC_{50,light}$ values of **3** and **NP3** were higher than

Table 6 Photocytotoxic activity of **1**, **3**, **NP1** and **NP3** in 2D and 3D cell cultures

2D-cultures	A549			HeLa		
	IC_{50} (μM)			IC_{50} (μM)		
	Dark	Light	PI	Dark	Light	PI
NP1	0.061 ± 0.0002	0.00086 ± 0.0004	70	0.069 ± 0.016	0.0024 ± 0.0011	28
NP3	1.79 ± 0.28	0.0415 ± 0.009	45	1.908 ± 0.27	0.0302 ± 0.0045	65

3D-cultures	A549		
	IC_{50} (μM)		
	Dark	Light	PI
1	5.10 ± 2.64	0.21 ± 0.08	24.3
NP1	1.44 ± 0.39	0.10 ± 0.03	14.4
3	38.78 ± 15.65	5.53 ± 0.01	7.0
NP3	>50.00	1.71 ± 0.53	>29.2

Cells were treated with the indicated complexes and NPs for 4 h at 37 °C and then kept in the dark or irradiated with blue light for 1 h (460 nm, 24.1 J cm^{-2}). Cell viability was assessed 43 h later by MTT assays (2D-cultures) or CellTiter Glo (3D-cultures). Data represent the mean ± SD. PI: phototoxicity index = $IC_{50,dark}/IC_{50,light}$.

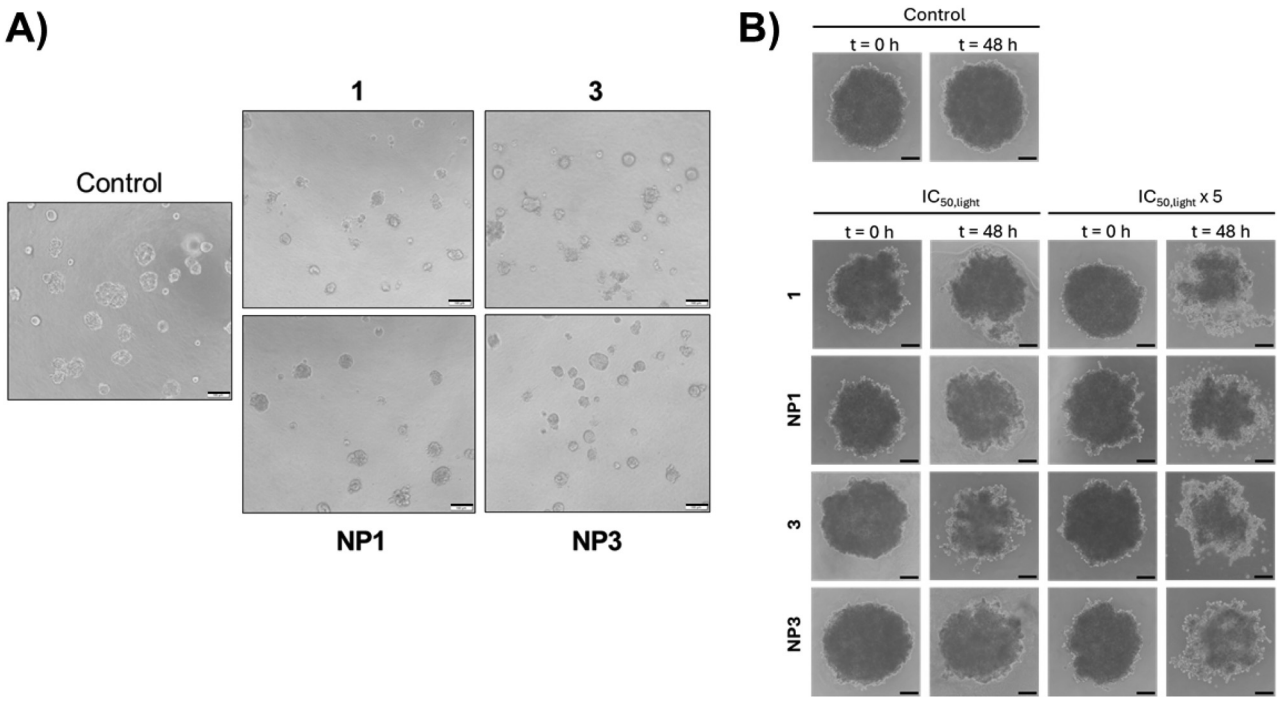

Fig. 12 Photocytotoxic activity against MCSs. (A) Representative microscopy images of A549 MCSs generated within the Geltrex extracellular matrix. Spheroids were treated under photoactivation conditions with complexes **1** and **3** at 0.3 μM and 10 μM, respectively, and nanoparticles **NP1** and **NP3**, at 0.2 μM and 2.7 μM, respectively. These concentrations are close to the $IC_{50,light}$ values for each compound. Untreated cells were used as a control. (B) Microscopy images of larger A549 MCSs generated in round-bottom wells with an ultra-low attachment surface. These MCSs were treated under photoactivation conditions with the complexes and nanoparticles at their $IC_{50,light}$ values (previously determined in the 3D models) or five times the $IC_{50,light}$. Images were acquired 43 h later (t = 48 h). Untreated spheroids served as a control (t = 0 h). Scale bars for all images: 100 μm.

those of **1** and **NP1**. It should be highlighted that **NP3** demonstrated minimal activity in the dark, leading to the highest PI value (>29.2) in MCSs.

To further corroborate these findings, an alternative 3D model was established to produce larger A549 MCSs with diameters of approximately 400 μm (Fig. 12B). These MCSs were treated with either the previously determined $IC_{50,light}$ values from the 3D models or with fivefold higher concentrations, followed by blue light irradiation. After 48 hours of treatment at the $IC_{50,light}$, MCSs exhibited reduced structural integrity and compactness compared with the control MCS images obtained before the treatment. Moreover, all MCSs exposed to fivefold the $IC_{50,light}$ showed a marked reduction in size and a highly disrupted morphology. These results align with those obtained using the earlier 3D model, further supporting the antitumor potential of the compounds.

To gain deeper insight into the impact of encapsulation on the biologic behavior of the complexes, cellular uptake studies were conducted using inductively coupled plasma mass spectrometry (ICP-MS) to quantify the amount of iridium inside the cells. The iridium levels were found to be 2.5- to 2.8 times higher in cells treated with **NP1** than with the free complex **1** (Fig. 13). These results aligned with the previously reported higher photocytotoxicity of **NP1**. In contrast, complex **3** and

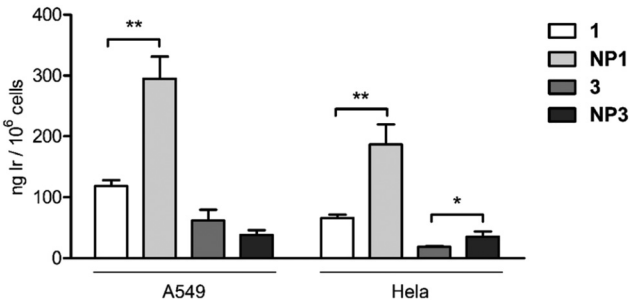

Fig. 13 Cellular internalization of complexes **1** and **3** and nanoparticles **NP1** and **NP3** in A549 and HeLa cells. The amount of iridium (ng) per million cells after 4 h of treatment was determined by ICP-MS. Each bar in the graph represents the mean ± SD of three independent experiments. * $p < 0.05$; ** $p < 0.01$.

NP3 exhibited lower cellular uptake. Encapsulation reduced the uptake of **3** in A549 cells; however a 1.9-fold higher internalization of **NP3** was detected in HeLa cells, which is in line with the relative values of photocytotoxicity observed for **3** and **NP3** in this cell line (Table 6).

Overall, these findings demonstrated a strong correlation between cellular internalization of the complexes and their antitumor efficacy. Interestingly, the higher lipophilicity of complex **1** ($\log P_{o/w} = 1.58 \pm 0.23$) than complex **3** ($\log P_{o/w} = 1.15 \pm 0.27$)

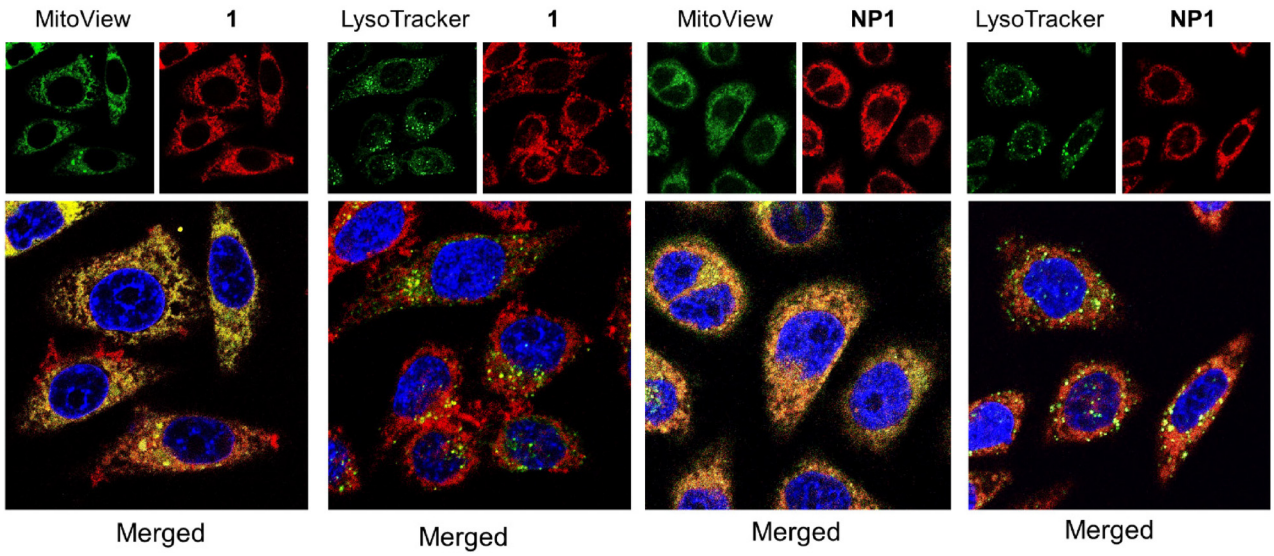

Fig. 14 Confocal microscopy imaging of the subcellular distribution of **1** and **NP1**. HeLa cells were incubated with **1** or **NP1** ($\lambda_{ex}/\lambda_{em}$: 440/596 nm) at 50 μg mL^{-1} for 1 h at 37 °C. The commercial dyes MitoView™ Green (Biotium) ($\lambda_{ex}/\lambda_{em}$: 490/523 nm) and LysoTracker™ Green DND-26 (ThermoFisher Scientific) ($\lambda_{ex}/\lambda_{em}$: 504/511 nm) and Hoechst ($\lambda_{ex}/\lambda_{em}$: 352/454 nm) were used to localize the mitochondria, lysosomes, and cell nuclei, respectively. Images were captured using a Nikon A1R confocal microscope using the following acquisition settings: blue channel: $\lambda_{ex}/\lambda_{em}$: 400/450 nm 33258, green channel: $\lambda_{ex}/\lambda_{em}$: 488/525 nm and red channel: $\lambda_{ex}/\lambda_{em}$: 488/595 nm. Merged images show the green and red fluorescence overlapping in orange.

correlated with an increased cellular accumulation. In addition, the smaller size of the pbpz ligand in complex **1** and its lower tendency to aggregate likely enhanced its cell penetration ability. Similar results have been reported with other Ir (III) complexes bearing π-extended N^N ligands analogous to the C^N pbpz and pbpn ligands used in the present work.[153]

Taking advantage of the luminescence properties of complex **1**, the internalization mechanism of its free and encapsulated forms was further explored by flow cytometry. A549 and HeLa cells were incubated with **1** and **NP1** for 4 h at either 37° or at 4 °C, to differentiate between energy-dependent and passive uptake processes. As illustrated in Fig. S84,† the fluorescence intensity was markedly reduced at 4 °C in comparison with 37 °C in both cell lines, suggesting that both complex **1** and **NP1** accumulate in the cells in an energy-dependent manner that involves active transport or endocytosis, rather than passive diffusion through the cell membrane.[154]

Subcellular distribution. Finally, the subcellular distribution of complex **1** and **NP1** was assessed using laser confocal microscopy. Microscopy images revealed a significant degree of co-localization between the red fluorescent signal of both complex **1** and **NP1** with MitoView™ Green, as shown in orange in the merged images (Fig. 14, and Fig. S85†). The Pearson's correlation coefficients (PCCs) were 0.75 for complex **1** and 0.76 for **NP1**. Mitochondrial accumulation is characteristic of these types of iridium complexes.[26] In contrast, the minimal degree of co-localization observed for **1** and for **NP1** with the lysosomal marker LysoTracker™ Green, with PCCs of 0.36 and 0.46 respectively, excluded these organelles as primary cellular targets. Nuclear localization was found to be negligible, as demonstrated by the absence of co-localization with the nuclear dye Hoechst 33258. It is noteworthy that encapsulation did not alter the subcellular distribution of complex **1**.

To confirm the mitochondrial localization of **1** and **NP1**, HeLa cells were incubated with each compound at 5 μM for 4 hours, followed by isolation of mitochondrial and residual cytosolic fractions using a commercial kit. Iridium content in both fractions was then quantified by ICP-MS. Complex **1** showed preferential accumulation in the mitochondria (0.964 μg Ir per mg protein) compared with the remaining cytosolic fraction (0.029 μg Ir per mg protein). Similarly, **NP1** exhibited a significantly higher mitochondrial concentration (3.16 μg Ir per mg protein) relative to the cytosolic fraction (0.014 μg Ir per mg protein). The increased mitochondrial iridium content observed in **NP1**-treated cells compared with cells treated with complex **1** is consistent with its higher overall cellular uptake, as illustrated in Fig. 13. Collectively, these findings confirm a strong tendency of both **1** and **NP1** to accumulate in the mitochondria.

3. Conclusions

Through a molecular design strategy and using innovative procedures we were able to obtain the new derivatives $[Ir(C^N)_2(bpy)]^+$ which include the π-expansive C^N ligands pbpz (complex **1**) or pbpn (complex **3**). The π-expansion led to an increase in the lifetimes of the excited states and a remarkable generation not only of $^1O_2$ but also of $O_2^{\bullet-}$, especially in the case of **1**. This allowed the complexes to act both by type II and

type I PDT processes. The generation of $O_2^{\bullet-}$ allows the circumvention of the problem of low O_2 content in some tumors.

The photophysical properties were notably affected by the degree of π-expansion of the C^N ligand, and TD-DFT studies, which found very different characteristics of the triplet excited states, nicely explained the divergences. In fact, **1** showed small energy differences among the four lowest triplet states enabling efficient ISC and RISC, promoting rapid interconversion within the triplet manifold. Consequently, compound **1** displayed delayed fluorescence, where the intersystem crossing between singlet and triplet states can extend the excited-state lifetime, enhancing its efficiency in reactive oxygen species (ROS) production. This phenomenon was not present in **3**. In this complex, the extra ring, in a similar way to that found in half-sandwich Ir(III) complexes with the pbpn ligand, causes the generation of two near-HOMO orbitals leading to a higher LC character of the excited states. Thus, lower degrees of SOC and ISC are found in **3** with respect to **1**. This rationale may be important in the design of new derivatives with improved properties.

Regarding anticancer activity, both complexes demonstrated notable phototoxicity against human cancer cells, both in monolayer and MCS cultures. It is noteworthy that in all cases, complex **1** demonstrated a markedly higher effect on cell viability than complex **3**. The complexes did not exhibit intrinsic selectivity for malignant cells. However, they demonstrated a high capacity to exert a selective light-activated action against cancer cells with minimal effects on non-irradiated healthy cells and erythrocytes. Upon photoactivation, both complexes induced a substantial increase in intracellular ROS levels, including the generation of superoxide anions. Cell confocal imaging revealed that complex **1** exhibited a marked accumulation in mitochondria, which correlated with the disruption of mitochondrial physiological functions, as evidenced by a decrease in mitochondrial membrane potential. Besides, complexes **1** and **3** were found to be among the most active NADH photocatalysts described to date. Wound healing and clonogenic assays demonstrated the capacity of the complexes to inhibit the spread of malignant cells and their capacity to generate secondary tumors, which are crucial steps in the metastatic process. These findings are promising, as metastasis is responsible for the greatest number of cancer-related deaths.

The encapsulation of the complexes into nanoparticles did not affect their photophysical properties. Moreover, it improved some of the drawbacks of the complexes such as aggregation and low solubility in water and low cellular uptake. Remarkably, the cellular uptake, even with low payload content, was improved by encapsulation and also the phototoxicity indexes were notably improved. Even in 3D cancer models this good behaviour was observed. **NP1** led to one of the lowest values of IC_{50} reported to date in iridium chemistry (0.86 nM). Thus, our strategy was successful, and the study points to the high potential of the pbpz and pbpn ligands, at least in iridium derivatives active in PDT processes. Complexes **1** and **3**, **NP1** and **NP3** show high promise as type I and II PDT agents that could also behave as theragnosis agents. Besides, there is also scope for further improving the properties by modifying the N^N ligand.

Conflicts of interest

There are no conflicts to declare.

Data availability

The data supporting this article have been included in the main text and as part of the ESI.†

Crystallographic data (CIF-files) have been uploaded to the CCDC and can be obtained *via* the CCDC homepage using the CCDC numbers provided in the manuscript.

Acknowledgements

This work was supported by the Spanish Ministerio de Ciencia, Innovación y Universidades (PID2021-127187OB-C21, PID2021-127187OB-C22), Junta de Comunidades de Castilla-La Mancha-FEDER (JCCM) (grant SBPLY/23/180225/000192), and UCLM-FEDER (grants 2019-GRIN-27183, 2019-GRIN-27209 and 2022-GRIN-34193). C. G. acknowledges his fellowship to both the European Social Fund and Plan Propio de I + D + I of UCLM (2022-PRED-20649). G. D. thanks the Junta de Comunidades de Castilla-La Mancha and EU for financial support through the European Regional Development Fund (project SBPLY/19/180501/000191). J. C. L. and A. M. acknowledge the Portuguese Foundation for Science and Technology for funding through LAQV-REQUIMTE (UIDB/50006/2020 and UIDP/50006/2020). C. B and E. Z. acknowledge their predoctoral grants University of Girona (IFUdG2021) and Generalitat de Catalunya (AGAUR; 2021 FI_B 01036). P. T. acknowledges national funds from FCT – Fundação para a Ciência e a Tecnologia (FCT-MCTES), I. P., in the scope of the project UIDB/04378/2020 of the Research Unit on Applied Molecular Biosciences – UCIBIO and LA/P/0140/2020 of the Associate Laboratory Institute for Health and Bioeconomy – i4HB. The collaboration of Prof. Antonio de la Hoz is acknowledged for the facilities to use the microwave system. The authors would like to thank the IRICA services at UCLM and Eduardo Prado García-Consuegra of the SEM services team for the technical assistance.

References

1 D. E. J. G. J. Dolmans, D. Fukumura and R. K. Jain, Photodynamic Therapy for Cancer, *Cancer*, 2003, **3**(5), 380–387, DOI: **10.1038/nrc1071**.

2 C. A. Robertson, D. H. Evans and H. Abrahamse, Photodynamic Therapy (PDT): A Short Review on Cellular Mechanisms and Cancer Research Applications for PDT,

J. Photochem. Photobiol., B, 2009, **96**(1), 1–8, DOI: 10.1016/j.jphotobiol.2009.04.001.

3 N. Mehraban and H. S. Freeman, Developments in PDT Sensitizers for Increased Selectivity and Singlet Oxygen Production, *Materials*, 2015, **8**(7), 4421–4456, DOI: 10.3390/ma8074421.

4 D. van Straten, V. Mashayekhi, H. de Bruijn, S. Oliveira and D. Robinson, Oncologic Photodynamic Therapy: Basic Principles, Current Clinical Status and Future Directions, *Cancers*, 2017, **9**(12), 19, DOI: 10.3390/cancers9020019.

5 A. P. Castano, T. N. Demidova and M. R. Hamblin, Mechanisms in Photodynamic Therapy: Part One - Photosensitizers, Photochemistry and Cellular Localization, *Photodiagn. Photodyn. Ther.*, 2004, **1**(4), 279–293, DOI: 10.1016/S1572-1000(05)00007-4.

6 M. Ju, L. Yang, G. Wang, F. Zong, Y. Shen, S. Wu, X. Tang and D. Yu, A Type I and Type II Chemical Biology Toolbox to Overcome the Hypoxic Tumour Microenvironment for Photodynamic Therapy, *Biomater. Sci.*, 2024, **12**(11), 2831–2840, DOI: 10.1039/d4bm00319e.

7 X. Li, J. F. Lovell, J. Yoon and X. Chen, Clinical Development and Potential of Photothermal and Photodynamic Therapies for Cancer, *Nat. Rev. Clin Oncol.*, 2020, **17**(11), 657–674, DOI: 10.1038/s41571-020-0410-2.

8 P. Agostinis, K. Berg, K. A. Cengel, T. H. Foster, A. W. Girotti, S. O. Gollnick, S. M. Hahn, M. R. Hamblin, A. Juzeniene, D. Kessel, M. Korbelik, J. Moan, P. Mroz, D. Nowis, J. Piette, B. C. Wilson and J. Golab, Photodynamic Therapy of Cancer: An Update, *CA Cancer J. Clin.*, 2011, **61**(4), 250–281, DOI: 10.3322/caac.20114.

9 A. B. Ormond and H. S. Freeman, Dye Sensitizers for Photodynamic Therapy, *Materials*, 2013, **6**(3), 817–840, DOI: 10.3390/ma6030817.

10 H. Huang, S. Banerjee and P. J. Sadler, Recent Advances in the Design of Targeted Iridium(III) Photosensitizers for Photodynamic Therapy, *ChemBioChem*, 2018, **19**(15), 1574–1589, DOI: 10.1002/cbic.201800182.

11 L. K. McKenzie, H. E. Bryant and J. A. Weinstein, Transition Metal Complexes as Photosensitisers in One- and Two-Photon Photodynamic Therapy, *Coord. Chem. Rev.*, 2019, **379**, 2–29, DOI: 10.1016/j.ccr.2018.03.020.

12 O. J. Stacey and S. J. A. Pope, New Avenues in the Design and Potential Application of Metal Complexes for Photodynamic Therapy, *RSC Adv.*, 2013, **3**(48), 25550, DOI: 10.1039/c3ra45219k.

13 J. Li and T. Chen, Transition Metal Complexes as Photosensitizers for Integrated Cancer Theranostic Applications, *Coord. Chem. Rev.*, 2020, **418**, 213355, DOI: 10.1016/j.ccr.2020.213355.

14 C. P. Tan, Y. M. Zhong, L. N. Ji and Z. W. Mao, Phosphorescent Metal Complexes as Theranostic Anticancer Agents: Combining Imaging and Therapy in a Single Molecule, *Chem. Sci.*, 2021, **12**(7), 2357–2367, DOI: 10.1039/d0sc06885c.

15 J. A. Roque, P. C. Barrett, H. D. Cole, L. M. Lifshits, G. Shi, S. Monro, D. Von Dohlen, S. Kim, N. Russo, G. Deep, C. G. Cameron, M. E. Alberto and S. A. McFarland, Breaking the Barrier: An Osmium Photosensitizer with Unprecedented Hypoxic Phototoxicity for Real World Photodynamic Therapy, *Chem. Sci.*, 2020, **11**(36), 9784–9806, DOI: 10.1039/d0sc03008b.

16 A. Kastl, S. Dieckmann, K. Wähler, T. Völker, L. Kastl, A. L. Merkel, A. Vultur, B. Shannan, K. Harms, M. Ocker, W. J. Parak, M. Herlyn and E. Meggers, Rhenium Complexes with Visible-Light-Induced Anticancer Activity, *ChemMedChem*, 2013, **8**(6), 924–927, DOI: 10.1002/cmdc.201300060.

17 F. Heinemann, J. Karges and G. Gasser, Critical Overview of the Use of Ru(II) Polypyridyl Complexes as Photosensitizers in One-Photon and Two-Photon Photodynamic Therapy, *Acc. Chem. Res.*, 2017, **50**(11), 2727–2736, DOI: 10.1021/acs.accounts.7b00180.

18 T. Sainuddin, J. McCain, M. Pinto, H. Yin, J. Gibson, M. Hetu and S. A. McFarland, Organometallic Ru(II) Photosensitizers Derived from π-Expansive Cyclometalating Ligands: Surprising Theranostic PDT Effects, *Inorg. Chem.*, 2016, **55**(1), 83–95, DOI: 10.1021/acs.inorgchem.5b01838.

19 S. Monro, K. L. Colón, H. Yin, J. Roque, P. Konda, S. Gujar, R. P. Thummel, L. Lilge, C. G. Cameron and S. A. McFarland, Transition Metal Complexes and Photodynamic Therapy from a Tumor-Centered Approach: Challenges, Opportunities, and Highlights from the Development of TLD1433, *Chem. Rev.*, 2019, **119**(2), 797–828, DOI: 10.1021/acs.chemrev.8b00211.

20 A. Zamora, G. Vigueras, V. Rodríguez, M. D. Santana and J. Ruiz, Cyclometalated Iridium(III) Luminescent Complexes in Therapy and Phototherapy, *Coord. Chem. Rev.*, 2018, **360**, 34–76, DOI: 10.1016/j.ccr.2018.01.010.

21 P. Y. Ho, C. L. Ho and W. Y. Wong, Recent Advances of Iridium(III) Metallophosphors for Health-Related Applications, *Coord. Chem. Rev.*, 2020, **413**, 213267, DOI: 10.1016/j.ccr.2020.213267.

22 R. Das, U. Das, N. Roy, C. Mukherjee, U. Sreelekha and P. Paira, A Glance on Target Specific PDT Active Cyclometalated Iridium Complexes, *Dyes Pigm.*, 2024, **226**, 112134, DOI: 10.1016/j.dyepig.2024.112134.

23 M. Ouyang, L. Zeng, K. Qiu, Y. Chen, L. Ji and H. Chao, Cyclometalated IrIII Complexes as Mitochondria-Targeted Photodynamic Anticancer Agents, *Eur. J. Inorg. Chem.*, 2017, **2017**(12), 1764–1771, DOI: 10.1002/ejic.201601129.

24 H. Huang, S. Banerjee and P. J. Sadler, Recent Advances in the Design of Targeted Iridium(III) Photosensitizers for Photodynamic Therapy, *ChemBioChem*, 2018, **19**(15), 1574–1589, DOI: 10.1002/cbic.201800182.

25 W. Lv, Z. Zhang, K. Y. Zhang, H. Yang, S. Liu, A. Xu, S. Guo, Q. Zhao and W. Huang, A Mitochondria-Targeted Photosensitizer Showing Improved Photodynamic Therapy Effects Under Hypoxia, *Angew. Chem., Int. Ed.*, 2016, **55**(34), 9947–9951, DOI: 10.1002/anie.201604130.

26 I. Echevarría, E. Zafon, S. Barrabés, M.Á Martínez, S. Ramos-Gómez, N. Ortega, B. R. Manzano, F. A. Jalón, R. Quesada, G. Espino and A. Massaguer, Rational Design of Mitochondria Targeted Thiabendazole-Based Ir(III) Biscyclometalated Complexes for a Multimodal Photodynamic Therapy of Cancer, *J. Inorg. Biochem.*, 2022, **231**, 111790, DOI: **10.1016/j.jinorgbio.2022.111790**.

27 K. K.-S. Tso and K. K.-W. Lo, Strategic Applications of Luminescent Iridium(III) Complexes as Biomolecular Probes, Cellular Imaging Reagents, and Photodynamic Therapeutics, in *Iridium(III) in Optoelectronic and Photonics Applications*, ed. E. Zysman-Colman, John Wiley & Sons Ltd, Chichester, UK, 2017. DOI: **10.1002/9781119007166.ch9**.

28 C. Reichardt, S. Monro, F. H. Sobotta, K. L. Colón, T. Sainuddin, M. Stephenson, E. Sampson, J. Roque, H. Yin, J. C. Brendel, C. G. Cameron, S. McFarland and B. Dietzek, Predictive Strength of Photophysical Measurements for in Vitro Photobiological Activity in a Series of Ru(II) Polypyridyl Complexes Derived from π-Extended Ligands, *Inorg. Chem.*, 2019, **58**(5), 3156–3166, DOI: **10.1021/acs.inorgchem.8b03223**.

29 L. M. Lifshits, J. A. Roque, P. Konda, S. Monro, H. D. Cole, D. Von Dohlen, S. Kim, G. Deep, R. P. Thummel, C. G. Cameron, S. Gujar and S. A. McFarland, Near-Infrared Absorbing Ru(II) Complexes Act as Immunoprotective Photodynamic Therapy (PDT) Agents against Aggressive Melanoma, *Chem. Sci.*, 2020, **11**(43), 11740–11762, DOI: **10.1039/d0sc03875j**.

30 H. Li, S. Liu, L. Lystrom, S. Kilina and W. Sun, Improving Triplet Excited-State Absorption and Lifetime of Cationic Iridium(III) Complexes by Extending π-Conjugation of the 2-(2-Quinolinyl) Quinoxaline Ligand, *J. Photochem. Photobiol., A*, 2020, **400**, 112609, DOI: **10.1016/j.jphotochem.2020.112609**.

31 B. Liu, S. Monro, Z. Li, M. A. Jabed, D. Ramirez, C. G. Cameron, K. Colón, J. Roque, S. Kilina, J. Tian, S. A. Mcfarland and W. Sun, New Class of Homoleptic and Heteroleptic Bis(Terpyridine) Iridium(III) Complexes with Strong Photodynamic Therapy Effects, *ACS Appl. Bio Mater.*, 2019, **2**(7), 2964–2977, DOI: **10.1021/acsabm.9b00312**.

32 L. Wang, S. Monro, P. Cui, H. Yin, B. Liu, C. G. Cameron, W. Xu, M. Hetu, A. Fuller, S. Kilina, S. A. McFarland and W. Sun, Heteroleptic Ir(III)N6 Complexes with Long-Lived Triplet Excited States and in Vitro Photobiological Activities, *ACS Appl. Mater. Interfaces*, 2019, **11**(4), 3629–3644, DOI: **10.1021/acsami.8b14744**.

33 Z. Li, P. Cui, C. Wang, S. Kilina and W. Sun, Nonlinear Absorbing Cationic Bipyridyl Iridium(III) Complexes Bearing Cyclometalating Ligands with Different Degrees of π-Conjugation: Synthesis, Photophysics, and Reverse Saturable Absorption, *J. Phys. Chem. C*, 2014, **118**(49), 28764–28775, DOI: **10.1021/jp5073457**.

34 R. Lincoln, L. Kohler, S. Monro, H. Yin, M. Stephenson, R. Zong, A. Chouai, C. Dorsey, R. Hennigar, R. P. Thummel and S. A. Mcfarland, Exploitation of Long-Lived 3IL Excited States for Metal – Organic Photodynamic Therapy : Verification in a Metastatic Melanoma Model, *J. Am. Chem. Soc.*, 2013, **135**, 17161–17175.

35 L. Wang, H. Yin, M. A. Jabed, M. Hetu, C. Wang, S. Monro, X. Zhu, S. Kilina, S. A. McFarland and W. Sun, π-Expansive Heteroleptic Ruthenium(II) Complexes as Reverse Saturable Absorbers and Photosensitizers for Photodynamic Therapy, *Inorg. Chem.*, 2017, **56**(6), 3245–3259, DOI: **10.1021/acs.inorgchem.6b02624**.

36 P. C. Barrett, S. M. A. Monro, T. Sainuddin, J. Mccain, K. L. Colo, J. Roque III, M. Pinto, H. Yin, C. G. Cameron and S. A. Mcfarland, Photophysical Properties and Photobiological Activities of Ruthenium(II) Complexes Bearing π - Expansive Cyclometalating Ligands with Thienyl Groups, *Inorg. Chem.*, 2019, **58**, 10778–10790, DOI: **10.1021/acs.inorgchem.9b01044**.

37 G. Ghosh, H. Yin, S. M. A. Monro, T. Sainuddin, L. Lapoot, A. Greer and S. A. Mcfarland, Synthesis and Characterization of Ru(II) Complexes with p -Expansive Imidazophen Ligands for the Photokilling of Human Melanoma Cells, *Photochem. Photobiol.*, 2020, **96**, 349–357, DOI: **10.1111/php.13177**.

38 M. D. Pozza, P. Mesdom, A. Abdullrahman, T. D. Prieto Otoya, P. Arnoux, C. Frochot, G. Niogret, B. Saubaméa, P. Burckel, J. P. Hall, M. Hollenstein, C. J. Cardin and G. Gasser, Increasing the π-Expansive Ligands in Ruthenium(II) Polypyridyl Complexes: Synthesis, Characterization, and Biological Evaluation for Photodynamic Therapy Applications, *Inorg. Chem.*, 2023, **62**(45), 18510–18523, DOI: **10.1021/acs.inorgchem.3c02606**.

39 L. M. Lifshits, J. A. Roque, P. Konda, S. Monro, H. D. Cole, D. Von Dohlen, S. Kim, G. Deep, R. P. Thummel, C. G. Cameron, S. Gujar and S. A. McFarland, Near-Infrared Absorbing Ru(II) Complexes Act as Immunoprotective Photodynamic Therapy (PDT) Agents against Aggressive Melanoma, *Chem. Sci.*, 2020, **11**(43), 11740–11762, DOI: **10.1039/d0sc03875j**.

40 B. Liu, S. Monro, Z. Li, M. A. Jabed, D. Ramirez, C. G. Cameron, K. Colón, J. Roque, S. Kilina, J. Tian, S. A. Mcfarland and W. Sun, New Class of Homoleptic and Heteroleptic Bis(Terpyridine) Iridium(III) Complexes with Strong Photodynamic Therapy Effects, *ACS Appl. Bio Mater.*, 2019, **2**(7), 2964–2977, DOI: **10.1021/acsabm.9b00312**.

41 L. Wang, S. Monro, P. Cui, H. Yin, B. Liu, C. G. Cameron, W. Xu, M. Hetu, A. Fuller, S. Kilina, S. A. McFarland and W. Sun, Heteroleptic Ir(III)N6 Complexes with Long-Lived Triplet Excited States and in Vitro Photobiological Activities, *ACS Appl. Mater. Interfaces*, 2019, **11**(4), 3629–3644, DOI: **10.1021/acsami.8b14744**.

42 C. Gonzalo-Navarro, E. Zafon, J. A. Organero, F. A. Jalón, J. C. Lima, G. Espino, A. M. Rodríguez, L. Santos, A. J. Moro, S. Barrabés, J. Castro, J. Camacho-Aguayo,

A. Massaguer, B. R. Manzano and G. Durá, Ir(III) Half-Sandwich Photosensitizers with a π-Expansive Ligand for Efficient Anticancer Photodynamic Therapy, *J. Med. Chem.*, 2024, **67**(3), 1783–1811, DOI: **10.1021/acs.jmedchem.3c01276**.

43 B. Yuan, J. Liu, R. Guan, C. Jin, L. Ji and H. Chao, Endoplasmic Reticulum Targeted Cyclometalated Iridium(III) Complexes as Efficient Photodynamic Therapy Photosensitizers, *Dalton Trans.*, 2019, **48**(19), 6408–6415, DOI: **10.1039/c9dt01072f**.

44 V. Novohradsky, G. Vigueras, J. Pracharova, N. Cutillas, C. Janiak, H. Kostrhunova, V. Brabec, J. Ruiz and J. Kasparkova, Molecular Superoxide Radical Photogeneration in Cancer Cells by Dipyridophenazine Iridium(III) Complexes, *Inorg. Chem. Front.*, 2019, **6**(9), 2500–2513, DOI: **10.1039/c9qi00811j**.

45 L. Markova, V. Novohradsky, J. Kasparkova, J. Ruiz and V. Brabec, Dipyridophenazine Iridium(III) Complex as a Phototoxic Cancer Stem Cell Selective, Mitochondria Targeting Agent, *Chem.-Biol. Interact.*, 2022, **360**, 109955, DOI: **10.1016/j.cbi.2022.109955**.

46 J. Kasparkova, A. Hernández-García, H. Kostrhunova, M. Goicuría, V. Novohradsky, D. Bautista, L. Markova, M. D. Santana, V. Brabec and J. Ruiz, Novel 2-(5-Arylthiophen-2-Yl)-Benzoazole Cyclometalated Iridium(III) Dppz Complexes Exhibit Selective Phototoxicity in Cancer Cells by Lysosomal Damage and Oncosis, *J. Med. Chem.*, 2024, **67**(1), 691–708, DOI: **10.1021/acs.jmedchem.3c01978**.

47 J. Liu, C. Jin, B. Yuan, Y. Chen, X. Liu, L. Ji and H. Chao, Enhanced Cancer Therapy by the Marriage of Metabolic Alteration and Mitochondrial-Targeted Photodynamic Therapy Using Cyclometalated Ir(III) Complexes, *Chem. Commun.*, 2017, **53**(71), 9878–9881, DOI: **10.1039/c7cc05518h**.

48 X. Tian, Y. Zhu, M. Zhang, L. Luo, J. Wu, H. Zhou, L. Guan, G. Battaglia and Y. Tian, Localization Matters: A Nuclear Targeting Two-Photon Absorption Iridium Complex in Photodynamic Therapy, *Chem. Commun.*, 2017, **53**(23), 3303–3306, DOI: **10.1039/C6CC09470H**.

49 J. Pracharova, G. Vigueras, V. Novohradsky, N. Cutillas, C. Janiak, H. Kostrhunova, J. Kasparkova, J. Ruiz and V. Brabec, Exploring the Effect of Polypyridyl Ligands on the Anticancer Activity of Phosphorescent Iridium(III) Complexes: From Proteosynthesis Inhibitors to Photodynamic Therapy Agents, *Chem. – Eur. J.*, 2018, **24**(18), 4607–4619, DOI: **10.1002/chem.201705362**.

50 X. D. Bi, R. Yang, Y. C. Zhou, D. Chen, G. K. Li, Y. X. Guo, M. F. Wang, D. Liu and F. Gao, Cyclometalated Iridium(III) Complexes as High-Sensitivity Two-Photon Excited Mitochondria Dyes and Near-Infrared Photodynamic Therapy Agents, *Inorg. Chem.*, 2020, **59**(20), 14920–14931, DOI: **10.1021/acs.inorgchem.0c01509**.

51 F. Xue, Y. Lu, Z. Zhou, M. Shi, Y. Yan, H. Yang and S. Yang, Two in One: Luminescence Imaging and 730 Nm Continuous Wave Laser Driven Photodynamic Therapy of Iridium Complexes, *Organometallics*, 2015, **34**(1), 73–77, DOI: **10.1021/om500895y**.

52 L. He, Y. Li, C. P. Tan, R. R. Ye, M. H. Chen, J. J. Cao, L. N. Ji and Z. W. Mao, Cyclometalated Iridium(III) Complexes as Lysosome-Targeted Photodynamic Anticancer and Real-Time Tracking Agents, *Chem. Sci.*, 2015, **6**(10), 5409–5418, DOI: **10.1039/c5sc01955a**.

53 K. Qiu, M. Ouyang, Y. Liu, H. Huang, C. Liu, Y. Chen, L. Ji and H. Chao, Two-Photon Photodynamic Ablation of Tumor Cells by Mitochondria-Targeted Iridium(III) Complexes in Aggregate States, *J. Mater. Chem. B*, 2017, **5**(27), 5488–5498, DOI: **10.1039/c7tb00731k**.

54 F. X. Wang, M. H. Chen, Y. N. Lin, H. Zhang, C. P. Tan, L. N. Ji and Z. W. Mao, Dual Functions of Cyclometalated Iridium(III) Complexes: Anti-Metastasis and Lysosome-Damaged Photodynamic Therapy, *ACS Appl. Mater. Interfaces*, 2017, **9**(49), 42471–42481, DOI: **10.1021/acsami.7b10258**.

55 Y. Li, K. N. Wang, L. He, L. N. Ji and Z. W. Mao, Synthesis, Photophysical and Anticancer Properties of Mitochondria-Targeted Phosphorescent Cyclometalated Iridium(III) N-Heterocyclic Carbene Complexes, *J. Inorg. Biochem.*, 2020, **205**, 110976, DOI: **10.1016/j.jinorgbio.2019.110976**.

56 S. P. Y. Li, C. T. S. Lau, M. W. Louie, Y. W. Lam, S. H. Cheng and K. K. W. Lo, Mitochondria-Targeting Cyclometalated Iridium(III)-PEG Complexes with Tunable Photodynamic Activity, *Biomaterials*, 2013, **34**(30), 7519–7532, DOI: **10.1016/j.biomaterials.2013.06.028**.

57 C. Wang, L. Lystrom, H. Yin, M. Hetu, S. Kilina, S. A. McFarland and W. Sun, Increasing the Triplet Lifetime and Extending the Ground-State Absorption of Biscyclometalated Ir(III) Complexes for Reverse Saturable Absorption and Photodynamic Therapy Applications, *Dalton Trans.*, 2016, **45**(41), 16366–16378, DOI: **10.1039/c6dt02416e**.

58 J. S. Nam, M. G. Kang, J. Kang, S. Y. Park, S. J. C. Lee, H. T. Kim, J. K. Seo, O. H. Kwon, M. H. Lim, H. W. Rhee and T. H. Kwon, Endoplasmic Reticulum-Localized Iridium(III) Complexes as Efficient Photodynamic Therapy Agents via Protein Modifications, *J. Am. Chem. Soc.*, 2016, **138**(34), 10968–10977, DOI: **10.1021/jacs.6b05302**.

59 F. Wei, F. Chen, S. Wu, M. Zha, J. Liu, K. L. Wong, K. Li and K. M. C. Wong, Ligand Regulation Strategy to Modulate ROS Nature in a Rhodamine-Iridium(III) Hybrid System for Phototherapy, *Inorg. Chem.*, 2024, **63**(13), 5872–5884, DOI: **10.1021/acs.inorgchem.3c04350**.

60 T. Kench, A. Rahardjo, G. G. Terrones, A. Bellamkonda, T. E. Maher, M. Storch, H. J. Kulik and R. Vilar, A Semi-Automated, High-Throughput Approach for the Synthesis and Identification of Highly Photo-Cytotoxic Iridium Complexes, *Angew. Chem., Int. Ed.*, 2024, **63**(18), e202401808, DOI: **10.1002/anie.202401808**.

61 X. D. Song, B. B. Chen, S. F. He, N. L. Pan, J. X. Liao, J. X. Chen, G. H. Wang and J. Sun, Guanidine-Modified Cyclometalated Iridium(III) Complexes for Mitochondria-Targeted Imaging and Photodynamic Therapy,

Eur. J. Med. Chem., 2019, **179**, 26–37, DOI: **10.1016/j.ejmech.2019.06.045**.

62 G. Vigueras, L. Markova, V. Novohradsky, A. Marco, N. Cutillas, H. Kostrhunova, J. Kasparkova, J. Ruiz and V. Brabec, A Photoactivated Ir(Iii) Complex Targets Cancer Stem Cells and Induces Secretion of Damage-Associated Molecular Patterns in Melanoma Cells Characteristic of Immunogenic Cell Death, *Inorg. Chem. Front.*, 2021, **8**(21), 4696–4711, DOI: **10.1039/d1qi00856k**.

63 L. Wang, H. Yin, P. Cui, M. Hetu, C. Wang, S. Monro, R. D. Schaller, C. G. Cameron, B. Liu, S. Kilina, S. A. McFarland and W. Sun, Near-Infrared-Emitting Heteroleptic Cationic Iridium Complexes Derived from 2,3-Diphenylbenzo[g] Quinoxaline as in Vitro Theranostic Photodynamic Therapy Agents, *Dalton Trans.*, 2017, **46**(25), 8091–8103, DOI: **10.1039/c7dt00913e**.

64 J. Liu, C. Jin, B. Yuan, X. Liu, Y. Chen, L. Ji and H. Chao, Selectively Lighting up Two-Photon Photodynamic Activity in Mitochondria with AIE-Active Iridium(III) Complexes, *Chem. Commun.*, 2017, **53**(12), 2052–2055, DOI: **10.1039/c6cc10015e**.

65 F. Wei, F. Chen, S. Wu, M. Zha, J. Liu, K. L. Wong, K. Li and K. M. C. Wong, Ligand Regulation Strategy to Modulate ROS Nature in a Rhodamine-Iridium(III) Hybrid System for Phototherapy, *Inorg. Chem.*, 2024, **63**(13), 5872–5884, DOI: **10.1021/acs.inorgchem.3c04350**.

66 G. Vigueras, L. Markova, V. Novohradsky, A. Marco, N. Cutillas, H. Kostrhunova, J. Kasparkova, J. Ruiz and V. Brabec, A Photoactivated Ir(Iii) Complex Targets Cancer Stem Cells and Induces Secretion of Damage-Associated Molecular Patterns in Melanoma Cells Characteristic of Immunogenic Cell Death, *Inorg. Chem. Front.*, 2021, **8**(21), 4696–4711, DOI: **10.1039/d1qi00856k**.

67 C. Wang, L. Lystrom, H. Yin, M. Hetu, S. Kilina, S. A. McFarland and W. Sun, Increasing the Triplet Lifetime and Extending the Ground-State Absorption of Biscyclometalated Ir(III) Complexes for Reverse Saturable Absorption and Photodynamic Therapy Applications, *Dalton Trans.*, 2016, **45**(41), 16366–16378, DOI: **10.1039/c6dt02416e**.

68 A. N. Al-jamal, A. F. Al-hussainy, B. Abdulrazzaq, H. Hussein, I. Mohammed, Z. Hassan, D. Kar, T. Muringayil and S. Thomas, Photodynamic Therapy (PDT) in Drug Delivery : Nano-Innovations Enhancing Treatment Outcomes, *Health Sci. Rev.*, 2025, **14**, 100218, DOI: **10.1016/j.hsr.2025.100218**.

69 S. Kwiatkowski, B. Knap, D. Przystupski, J. Saczko, E. Kędzierska, K. Knap-Czop, J. Kotlińska, O. Michel, K. Kotowski and J. Kulbacka, Photodynamic Therapy – Mechanisms, Photosensitizers and Combinations, *Biomed. Pharmacother.*, 2018, **106**, 1098–1107, DOI: **10.1016/j.biopha.2018.07.049**.

70 J. Bonelli, E. Ortega-Forte, G. Vigueras, M. Bosch, N. Cutillas, J. Rocas, J. Ruiz and V. Marchán, Polyurethane-Polyurea Hybrid Nanocapsules as Efficient Delivery Systems of Anticancer Ir(III) Metallodrugs, *Inorg. Chem. Front.*, 2022, **9**(10), 2123–2138, DOI: **10.1039/d1qi01542g**.

71 Z. Feng, P. Tao, L. Zou, P. Gao, Y. Liu, X. Liu, H. Wang, S. Liu, Q. Dong, J. Li, B. Xu, W. Huang, W. Y. Wong and Q. Zhao, Hyperbranched Phosphorescent Conjugated Polymer Dots with Iridium(III) Complex as the Core for Hypoxia Imaging and Photodynamic Therapy, *ACS Appl. Mater. Interfaces*, 2017, **9**(34), 28319–28330, DOI: **10.1021/acsami.7b09721**.

72 V. R. Shinde, N. Revi, S. Murugappan, S. P. Singh and A. K. Rengan, Enhanced Permeability and Retention Effect: A Key Facilitator for Solid Tumor Targeting by Nanoparticles, *Photodiagn. Photodyn. Ther.*, 2022, **39**, 102915, DOI: **10.1016/j.pdpdt.2022.102915**.

73 D. Kalyane, N. Raval, R. Maheshwari, V. Tambe, K. Kalia and R. K. Tekade, Employment of Enhanced Permeability and Retention Effect (EPR): Nanoparticle-Based Precision Tools for Targeting of Therapeutic and Diagnostic Agent in Cancer, *Mater. Sci. Eng., C*, 2019, **98**, 1252–1276, DOI: **10.1016/j.msec.2019.01.066**.

74 J. Bonelli, E. Ortega-Forte, G. Vigueras, M. Bosch, N. Cutillas, J. Rocas, J. Ruiz and V. Marchán, Polyurethane-Polyurea Hybrid Nanocapsules as Efficient Delivery Systems of Anticancer Ir(III) Metallodrugs, *Inorg. Chem. Front.*, 2022, **9**(10), 2123–2138, DOI: **10.1039/d1qi01542g**.

75 C.-C. Lin and A. T. Metters, Hydrogels in Controlled Release Formulations: Network Design and Mathematical Modeling, *Adv. Drug Delivery Rev.*, 2006, **58**(12–13), 1379–1408, DOI: **10.1016/j.addr.2006.09.004**.

76 S. Fujii, Polymeric Core-Crosslinked Particles Prepared via a Nanoemulsion- Mediated Process: From Particle Design and Structural Characterization to in Vivo Behavior in Chemotherapy, *Polym. J.*, 2023, **55**, 921–933, DOI: **10.1038/s41428-023-00793-6**.

77 J. S. Lee and J. Feijen, Polymersomes for Drug Delivery : Design, Formation and Characterization, *J. Controlled Release*, 2012, **161**(2), 473–483, DOI: **10.1016/j.jconrel.2011.10.005**.

78 H. Wu and C. Wang, Biodegradable Smart Nanogels : A New Platform for Targeting Drug Delivery and Biomedical Diagnostics, *Langmuir*, 2016, **32**, 6211–6225, DOI: **10.1021/acs.langmuir.6b00842**.

79 R. K. O. Reilly, J. Hawker, K. L. Wooley and R. K. O. Reilly, Cross-Linked Block Copolymer Micelles : Functional Nanostructures of Great Potential and Versatility, *Chem. Soc. Rev.*, 2006, **35**, 1068–1083, DOI: **10.1039/b514858h**.

80 C. Liao, Y. Chen, Y. Yao, S. Zhang, Z. Gu and X. Yu, Cross-Linked Small-Molecule Micelle-Based Drug Delivery System: Concept, Synthesis, and Biological Evaluation, *Chem. Mater.*, 2016, **28**, 7757–7764, DOI: **10.1021/acs.chemmater.6b02965**.

81 B. Yuan, J. Liu, R. Guan, C. Jin, L. Ji and H. Chao, Endoplasmic Reticulum Targeted Cyclometalated Iridium(III) Complexes as Efficient Photodynamic Therapy

Photosensitizers, *Dalton Trans.*, 2019, **48**(19), 6408–6415, DOI: 10.1039/c9dt01072f.

82 M. Nonoyama, Benzo[h]Quinolin-10-Yl- N Iridium(III) Complexes, *Bull. Chem. Soc. Jpn.*, 1974, 767–768, DOI: 10.1246/bcsj.47.767.

83 S. Sprouse, K. A. King, P. J. Spellane and R. J. Watts, Photophysical Effects of Metal-Carbon σ Bonds in Ortho-Metalated Complexes of Ir(III) and Rh(III), *J. Am. Chem. Soc.*, 1984, **106**(22), 6647–6653, DOI: 10.1021/ja00334a031.

84 K. W. Jennette, J. T. Gill, J. A. Sadownick and S. J. Lippard, Metallointercalation Reagents., Synthesis, Characterization, and Structural Properties of Thiolato(2,2′,2″-Terpyridine) Platinum(II) Complexes, *J. Am. Chem. Soc.*, 1976, **98**(20), 6159–6168, DOI: 10.1021/ja00436a016.

85 V. V. Sivchik, E. V. Grachova, A. S. Melnikov, S. N. Smirnov, A. Y. Ivanov, P. Hirva, S. P. Tunik and I. O. Koshevoy, Solid-State and Solution Metallophilic Aggregation of a Cationic [Pt(NCN)L]+ Cyclometalated Complex, *Inorg. Chem.*, 2016, **55**(7), 3351–3363, DOI: 10.1021/acs.inorgchem.5b02713.

86 K. W. Jennette, J. T. Gill, J. A. Sadownick and S. J. Lippard, Metallointercalation Reagents., Synthesis, Characterization, and Structural Properties of Thiolato (2,2′,2″-Terpyridine)Platinum(II) Complexes, *J. Am. Chem. Soc.*, 1976, **98**(20), 6159–6168, DOI: 10.1021/ja00436a016.

87 M. Vaquero, A. Ruiz-Riaguas, M. Martínez-Alonso, F. A. Jalón, B. R. Manzano, A. M. Rodríguez, G. García-Herbosa, A. Carbayo, B. García and G. Espino, Selective Photooxidation of Sulfides Catalyzed by Bis-Cyclometalated IrIII Photosensitizers Bearing 2,2′-Dipyridylamine-Based Ligands, *Chem. – Eur. J.*, 2018, **24**(42), 10662–10671, DOI: 10.1002/chem.201801173.

88 M. Martínez-Alonso, N. Busto, L. D. Aguirre, L. Berlanga, M. C. Carrión, J. V. Cuevas, A. M. Rodríguez, A. Carbayo, B. R. Manzano, E. Ortí, F. A. Jalón, B. García and G. Espino, Strong Influence of the Ancillary Ligand over the Photodynamic Anticancer Properties of Neutral Biscyclometalated Ir III Complexes Bearing 2-Benzoazole-Phenolates, *Chem. – Eur. J.*, 2018, **24**(66), 17523–17537, DOI: 10.1002/chem.201803784.

89 J. Sanz-Villafruela, C. Martínez-Alonso, I. Echevarría, M. Vaquero, A. Carbayo, J. Fidalgo, A. M. Rodríguez, J. V. Cuevas-Vicario, J. C. Lima, A. J. Moro, B. R. Manzano, F. A. Jalón and G. Espino, One-Pot Photocatalytic Transformation of Indolines into 3-Thiocyanate Indoles with New Ir(III) Photosensitizers Bearing β-Carbolines, *Inorg. Chem. Front.*, 2021, **8**(5), 1253–1270, DOI: 10.1039/d0qi01307b.

90 E. Zafon, I. Echevarría, S. Barrabés, B. R. Manzano, F. A. Jalón, A. M. Rodríguez, A. Massaguer and G. Espino, Photodynamic Therapy with Mitochondria-Targeted Biscyclometallated Ir(III) Complexes. Multi-Action Mechanism and Strong Influence of the Cyclometallating Ligand, *Dalton Trans.*, 2022, **51**(1), 111–128, DOI: 10.1039/d1dt03080a.

91 J. Kasparkova, A. Hernández-García, H. Kostrhunova, M. Goicuría, V. Novohradsky, D. Bautista, L. Markova, M. D. Santana, V. Brabec and J. Ruiz, Novel 2-(5-Arylthiophen-2-Yl)-Benzoazole Cyclometalated Iridium(III) Dppz Complexes Exhibit Selective Phototoxicity in Cancer Cells by Lysosomal Damage and Oncosis, *J. Med. Chem.*, 2024, **67**(1), 691–708, DOI: 10.1021/acs.jmedchem.3c01978.

92 V. W. W. Yam, K. K. W. Lo, K. K. Cheung and R. Y. C. Kong, Deoxyribonucleic Acid Binding and Photocleavage Studies of Rhenium(I) Dipyridophenazine Complexes, *J. Chem. Soc., Dalton Trans.*, 1997, **14**(12), 2067–2072, DOI: 10.1039/a700828g.

93 D. Herebian and W. S. Sheldrick, Synthesis and DNA Binding Properties of Bioorganometallic (H5-Pentamethylcyclopentadienyl)Iridium(III) Complexes of the Type [(H5-C5Me5)Ir(Aa)(Dppz)]N+ (Dppz = Dipyrido [3,2-a:2′,3′-c]Phenazine, n = 1–3), with S-Coordinated Amino Acids (Aa) or Peptides, *J. Chem. Soc., Dalton Trans.*, 2002, (6), 966–974, DOI: 10.1039/b107656f.

94 A. Frodl, D. Herebian and W. S. Sheldrick, Coligand Tuning of the DNA Binding Properties of Bioorgano-Metallic (H6-Arene)Ruthenium(II) Complexes of the Type [(H6-Arene)-Ru(Amino Acid)(Dppz)]N+(Dppz = Dipyrido [3,2-a:2′,3′-c]Phenazine), n = 1-3, *J. Chem. Soc., Dalton Trans.*, 2002, (19), 3664–3673, DOI: 10.1039/b203569n.

95 K. K. W. Lo, C. K. Chung and N. Zhu, Nucleic Acid Intercalators and Avidin Probes Derived from Luminescent Cyclometalated Iridium(III)-Dipyridoquinoxaline and -Dipyridophenazine Complexes, *Chem. – Eur. J.*, 2006, **12**(5), 1500–1512, DOI: 10.1002/chem.200500885.

96 A. S. Shetty, J. Zhang and J. S. Moore, Aromatic π-Stacking in Solution as Revealed through the Aggregation of Phenylacetylene Macrocycles, *J. Am. Chem. Soc.*, 1996, **118**(5), 1019–1027, DOI: 10.1021/ja9528893.

97 M. C. Carrión, G. Durá, F. A. Jalón, B. R. Manzano and A. M. Rodríguez, Polynuclear Complexes Containing Ditopic Bispyrazolylmethane Ligands. Influence of Metal Geometry and Supramolecular Interactions, *Cryst. Growth Des.*, 2012, **12**(4), 1952–1969, DOI: 10.1021/cg201677s.

98 X. Yang, L. Cheng, Y. Zhao, H. Ma, H. Song, X. Yang, K. N. Wang and Y. Zhang, Aggregation-Induced Emission-Active Iridium(III)-Based Mitochondria-Targeting Nanoparticle for Two-Photon Imaging-Guided Photodynamic Therapy, *J. Colloid Interface Sci.*, 2024, **659**, 320–329, DOI: 10.1016/j.jcis.2023.12.172.

99 J. Mosinger, M. Janošková, K. Lang and P. Kubát, Light-Induced Aggregation of Cationic Porphyrins, *J. Photochem. Photobiol., A*, 2006, **181**(2–3), 283–289, DOI: 10.1016/j.jphotochem.2005.12.009.

100 R. G. Antoneli, T. B. F. Moraes, H. C. Junqueira, L. M. Sihn, H. E. Toma, B. Pedras, L. F. V. Ferreira, D. Frath, C. Bucher, J. W. Steed, G. J. F. Demets and E. R. Triboni, Unprecedented Light Induced Aggregation of Cationic 1,4,5,8-Naphthalenediimide Amphiphiles, *J. Mater. Chem. C*, 2024, **12**(11), 3888–3896, DOI: 10.1039/d3tc04178f.

101 K. Qiu, M. Ouyang, Y. Liu, H. Huang, C. Liu, Y. Chen, L. Ji and H. Chao, Two-Photon Photodynamic Ablation of Tumor Cells by Mitochondria-Targeted Iridium(III) Complexes in Aggregate States, *J. Mater. Chem. B*, 2017, **5**(27), 5488–5498, DOI: **10.1039/c7tb00731k**.

102 M. S. Lowry, W. R. Hudson, R. A. Pascal and S. Bernhard, Accelerated Luminophore Discovery through Combinatorial Synthesis, *J. Am. Chem. Soc.*, 2004, **126**(43), 14129–14135, DOI: **10.1021/ja047156+**.

103 J. M. Wessels, C. S. Foote, W. E. Ford and M. A. J. Rodgers, Photooxidation of Tryptophan: O2(1Δ*g*) versus Electron-Transfer Pathway, *Photochem. Photobiol.*, 1997, **65**(1), 96–102, DOI: **10.1111/j.1751-1097.1997.tb01883.x**.

104 D. Blasco, J. M. López-De-Luzuriaga, M. Monge, M. E. Olmos, D. Pascual and M. Rodríguez-Castillo, Time-Dependent Molecular Rearrangement of [Au(N9-Adeninate)(PTA)] in Aqueous Solution and Aggregation-Induced Emission in a Hydrogel Matrix, *Inorg. Chem.*, 2021, **60**(6), 3667–3676, DOI: **10.1021/acs.inorgchem.0c03291**.

105 S. Tofighi, P. Zhao, R. M. O'Donnell, J. Shi, P. Y. Zavalij, M. V. Bondar, D. J. Hagan and E. W. Van Stryland, Fast Triplet Population in Iridium(III) Complexes with Less than Unity Singlet to Triplet Quantum Yield, *J. Phys. Chem. C*, 2019, **123**(22), 13846–13855, DOI: **10.1021/acs.jpcc.9b00539**.

106 C. Grewer and H.-D. Brauer, Mechanism of the Triplet-State Quenching by Molecualr Oxygen in Solution, *J. Phys. Chem.*, 1994, **98**, 4230–4235.

107 C. Huang, C. Liang, T. Sadhukhan, S. Banerjee, Z. Fan, T. Li, Z. Zhu, P. Zhang, K. Raghavachari and H. Huang, In vitro and In vivo Photocatalytic Cancer Therapy with Biocompatible Iridium(III) Photocatalysts, *Angew. Chem., Int. Ed.*, 2021, **60**(17), 9474–9479, DOI: **10.1002/anie.202015671**.

108 J. S. Nam, M. G. Kang, J. Kang, S. Y. Park, S. J. C. Lee, H. T. Kim, J. K. Seo, O. H. Kwon, M. H. Lim, H. W. Rhee and T. H. Kwon, Endoplasmic Reticulum-Localized Iridium(III) Complexes as Efficient Photodynamic Therapy Agents via Protein Modifications, *J. Am. Chem. Soc.*, 2016, **138**(34), 10968–10977, DOI: **10.1021/jacs.6b05302**.

109 J. M. Wessels, C. S. Foote, W. E. Ford and M. A. J. Rodgers, Photooxidation of Tryptophan: O2(1Δ*g*) versus Electron-Transfer Pathway, *Photochem. Photobiol.*, 1997, **65**(1), 96–102, DOI: **10.1111/j.1751-1097.1997.tb01883.x**.

110 V. Novohradsky, G. Vigueras, J. Pracharova, N. Cutillas, C. Janiak, H. Kostrhunova, V. Brabec, J. Ruiz and J. Kasparkova, Molecular Superoxide Radical Photogeneration in Cancer Cells by Dipyridophenazine Iridium(III) Complexes, *Inorg. Chem. Front.*, 2019, **6**(9), 2500–2513, DOI: **10.1039/c9qi00811j**.

111 J. Moan and E. Wold, Detection of singlet oxygen production by ESR, *Nature*, 1979, **279**, 450–451, DOI: **10.1038/279450a0**.

112 Y. Tian, Y. Li, Y. Li, Z. Zhao, G. G. Ying, K. Shih and Y. Feng, New Insights into the Singlet Oxygen-Independent Formation of TEMPO Signals in Electron Paramagnetic Resonance Analysis, *Sep. Purif. Technol.*, 2025, **355**, 129564, DOI: **10.1016/j.seppur.2024.129564**.

113 S. Zhu, X. Li, J. Kang, X. Duan and S. Wang, Persulfate Activation on Crystallographic Manganese Oxides: Mechanism of Singlet Oxygen Evolution for Nonradical Selective Degradation of Aqueous Contaminants, *Environ. Sci. Technol.*, 2019, **53**(1), 307–315, DOI: **10.1021/acs.est.8b04669**.

114 E. Finkelstein, G. M. Rosen and E. J. Rauckman, *Spin Trapping of Superoxide and Hydroxyl Radical: Practical Aspects*, 1980, Vol. 200.

115 N. P. Truong, G. R. Jones, K. G. E. Bradford, D. Konkolewicz and A. Anastasaki, A Comparison of RAFT and ATRP Methods for Controlled Radical Polymerization, *Nat. Rev. Chem.*, 2021, **5**, 859–869, DOI: **10.1038/s41570-021-00328-8**.

116 J. S. Suk, Q. Xu, N. Kim, J. Hanes and L. M. Ensign, PEGylation as a Strategy for Improving Nanoparticle-Based Drug and Gene Delivery, *Adv. Drug Delivery Rev.*, 2016, **99**, 28–51, DOI: **10.1016/j.addr.2015.09.012**.

117 L. Fu, L. Liu, Z. Ruan, H. Zhang and L. Yan, Folic Acid Targeted PH-Responsive Amphiphilic Polymer Nanoparticles Conjugated with near Infrared Fluorescence Probe for Imaging-Guided Drug Delivery, *RSC Adv.*, 2016, **6**(46), 40312–40322, DOI: **10.1039/C6RA05657A**.

118 H. H. Schmidtke, Vibrational progressions in electronic spectra of complex compounds indicating strong vibronic coupling, in *Electronic and Vibronic Spectra of Transition Metal Complexes I, Topics in Current Chemistry*, ed. H. Yersin, 1994, vol. 171, Springer, Berlin, Heidelberg, DOI: **10.1007/3-540-58155-3_3**.

119 A. P. Demchenko, V. I. Tomin and P. T. Chou, Breaking the Kasha Rule for More Efficient Photochemistry, *Chem. Rev.*, 2017, **117**(21), 13353–13381, DOI: **10.1021/acs.chemrev.7b00110**.

120 J. U. Kim, I. S. Park, C. Y. Chan, M. Tanaka, Y. Tsuchiya, H. Nakanotani and C. Adachi, Nanosecond-Time-Scale Delayed Fluorescence Molecule for Deep-Blue OLEDs with Small Efficiency Rolloff, *Nat. Commun.*, 2020, **11**(1), 1765, DOI: **10.1038/s41467-020-15558-5**.

121 M. J. G. Peach and D. J. Tozer, Overcoming Low Orbital Overlap and Triplet Instability Problems in TDDFT, *J. Phys. Chem. A*, 2012, **116**, 9783–9789, DOI: **10.1021/jp308662x**.

122 M. J. G. Peach, M. J. Williamson and D. J. Tozer, Influence of Triplet Instabilities in TDDFT, *J. Chem. Theory Comput.*, 2011, **7**(11), 3578–3585, DOI: **10.1021/ct200651r**.

123 J. Zhang, Y. Wang, J. Ma, L. Jin and F. Liu, Density Functional Theory Investigation on Iridium(III) Complexes for Efficient Blue Electrophosphorescence, *RSC Adv.*, 2018, **4**, 19437–19448, DOI: **10.1039/c8ra02858c**.

124 Y. Y. Pan, J. Huang, Z. M. Wang, D. W. Yu, B. Yang and Y. G. Ma, Computational Investigation on the Large Energy Gap between the Triplet Excited-States in Acenes, *RSC Adv.*, 2017, **7**, 26697–26703, DOI: **10.1039/c7ra02559a**.

125 I. Ashur, R. Goldschmidt, I. Pinkas, Y. Salomon, G. Szewczyk, T. Sarna and A. Scherz, Photocatalytic Generation of Oxygen Radicals by the Water-Soluble Bacteriochlorophyll Derivative WST1 l, Noncovalently Bound to Serum Albumin, *J. Phys. Chem. A*, 2009, **113**(28), 8027–8037, DOI: **10.1021/jp900580e**.

126 Kenry, C. Chen and B. Liu, Enhancing the Performance of Pure Organic Room-Temperature Phosphorescent Luminophores, *Nat. Commun.*, 2019, **10**(1), 2111, DOI: **10.1038/s41467-019-10033-2**.

127 J. Li, T. Tian, D. Guo, T. Li, M. Zhang and H. Zhang, Importance of Spin-Triplet Excited-State Character in the Reverse Intersystem Crossing Process of Spiro-Based TADF Emitters, *J. Mater. Chem. C*, 2023, **11**(18), 6119–6129, DOI: **10.1039/d2tc05402g**.

128 P. Pander, R. Motyka, P. Zassowski, M. K. Etherington, D. Varsano, T. J. Da Silva, M. J. Caldas, P. Data and A. P. Monkman, Thermally Activated Delayed Fluorescence Mediated through the Upper Triplet State Manifold in Non-Charge-Transfer Star-Shaped Triphenylamine-Carbazole Molecules, *J. Phys. Chem. C*, 2018, **122**(42), 23934–23942, DOI: **10.1021/acs.jpcc.8b07610**.

129 C. Ash, M. Dubec, K. Donne and T. Bashford, Effect of Wavelength and Beam Width on Penetration in Light-Tissue Interaction Using Computational Methods, *Lasers Med. Sci.*, 2017, **32**(8), 1909–1918, DOI: **10.1007/s10103-017-2317-4**.

130 I. Sæbø, M. Bjørås, H. Franzyk, E. Helgesen and J. Booth, Optimization of the Hemolysis Assay for the Assessment of Cytotoxicity, *Int. J. Mol. Sci.*, 2023, **24**(3), 2914, DOI: **10.3390/ijms24032914**.

131 N. A. P. Franken, H. M. Rodermond, J. Stap, J. Haveman and C. van Bree, Clonogenic Assay of Cells in Vitro, *Nat. Protoc.*, 2006, **1**(5), 2315–2319, DOI: **10.1038/nprot.2006.339**.

132 L. Yu, Z. Liu, W. Xu, K. Jin, J. Liu, X. Zhu, Y. Zhang and Y. Wu, Towards Overcoming Obstacles of Type II Photodynamic Therapy: Endogenous Production of Light, Photosensitizer, and Oxygen, *Acta Pharm. Sin. B*, 2024, **14**(3), 1111–1131, DOI: **10.1016/j.apsb.2023.11.007**.

133 Z. Zhou, J. Song, L. Nie and X. Chen, Reactive Oxygen Species Generating Systems Meeting Challenges of Photodynamic Cancer Therapy, *Chem. Soc. Rev.*, 2016, **45**(23), 6597–6626, DOI: **10.1039/c6cs00271d**.

134 M. D. Brand, The Sites and Topology of Mitochondrial Superoxide Production, *Exp. Gerontol.*, 2010, **45**(7–8), 466–472, DOI: **10.1016/j.exger.2010.01.003**.

135 H. Vakifahmetoglu-Norberg, A. T. Ouchida and E. Norberg, The Role of Mitochondria in Metabolism and Cell Death, *Biochem. Biophys. Res. Commun.*, 2017, **482**(3), 426–431, DOI: **10.1016/j.bbrc.2016.11.088**.

136 S. Altenhöfer, K. A. Radermacher, P. W. M. Kleikers, K. Wingler and H. H. H. W. Schmidt, Evolution of NADPH Oxidase Inhibitors: Selectivity and Mechanisms for Target Engagement, *Antioxid. Redox Signal.*, 2015, **23**(5), 406–427, DOI: **10.1089/ars.2013.5814**.

137 H. Huang, S. Banerjee, K. Qiu, P. Zhang, O. Blacque, T. Malcomson, M. J. Paterson, G. J. Clarkson, M. Staniforth, V. G. Stavros, G. Gasser, H. Chao and P. J. Sadler, Targeted Photoredox Catalysis in Cancer Cells, *Nat. Chem.*, 2019, **11**(11), 1041–1048, DOI: **10.1038/s41557-019-0328-4**.

138 Z. Liu, I. Romero-Canelón, B. Qamar, J. M. Hearn, A. Habtemariam, N. P. E. Barry, A. M. Pizarro, G. J. Clarkson and P. J. Sadler, The Potent Oxidant Anticancer Activity of Organoiridium Catalysts, *Angew. Chem., Int. Ed.*, 2014, **53**(15), 3941–3946, DOI: **10.1002/anie.201311161**.

139 Z. Liu, R. J. Deeth, J. S. Butler, A. Habtemariam, M. E. Newton and P. J. Sadler, Reduction of Quinones by NADH Catalyzed by Organoiridium Complexes, *Angew. Chem., Int. Ed.*, 2013, **52**(15), 4194–4197, DOI: **10.1002/anie.201300747**.

140 X. Liu, X. He, X. Zhang, Y. Wang, J. Liu and X. Hao, New Organometallic Tetraphenylethylene · Iridium(III) Complexes with Antineoplastic Activity, *ChemBioChem*, 2019, **2767**, 2767–2776, DOI: **10.1002/cbic.201900268**.

141 J. Foreman, V. Demidchik, J. H. F. Bothwell, P. Mylona, H. Miedema, M. Angel Torres, P. Linstead, S. Costa, C. Brownlee, J. D. G. Jones, J. M. Davies and L. Dolan, Reactive Oxygen Species Produced by NADPH Oxidase Regulate Plant Cell Growth, *Nature*, 2003, **422**(6930), 442–446, DOI: **10.1038/nature01485**.

142 S. Fulda and K.-M. Debatin, Extrinsic versus Intrinsic Apoptosis Pathways in Anticancer Chemotherapy, *Oncogene*, 2006, **25**, 4798–4811, DOI: **10.1038/sj.onc.1209608**.

143 Y. Li, B. Liu, Y. Zheng, M. Hu, L.-Y. Liu, C.-R. Li, W. Zhang, Y.-X. Lai and Z.-W. Mao, Photoinduction of Ferroptosis and CGAS-STING Activation by a H 2 S-Responsive Iridium(III) Complex for Cancer-Specific Therapy, *J. Med. Chem.*, 2024, **67**, 16235–16247, DOI: **10.1021/acs.jmedchem.4c01065**.

144 H. Zhang, X. Liao, X. Wu, C. Shi, Y. Zhang, Y. Yuan, W. Li, J. Wang and Y. Liu, Iridium(III) Complexes Entrapped in Liposomes Trigger Mitochondria-Mediated Apoptosis and GSDME-Mediated Pyroptosis, *J. Inorg. Biochem.*, 2022, **228**, 111706, DOI: **10.1016/j.jinorgbio.2021.111706**.

145 H. Yuan, Z. Han, Y. Chen, F. Qi, H. Fang, Z. Guo, S. Zhang and W. He, Ferroptosis Photoinduced by New Cyclometalated Iridium(III) Complexes and Its Synergism with Apoptosis in Tumor Cell Inhibition, *Angew. Chem., Int. Ed.*, 2021, **60**(15), 8174–8181, DOI: **10.1002/anie.202014959**.

146 T. V. Denisenko, A. S. Gorbunova and B. Zhivotovsky, Mitochondrial Involvement in Migration, Invasion and Metastasis, *Front. Cell Dev. Biol.*, 2019, **7**, DOI: **10.3389/fcell.2019.00355**.

147 J. Fares, M. Y. Fares, H. H. Khachfe, H. A. Salhab and Y. Fares, Molecular Principles of Metastasis: A Hallmark

of Cancer Revisited, *Signal Transduction Targeted Ther.*, 2020, **5**(1), 28, DOI: **10.1038/s41392-020-0134-x**.

148 V. R. Shinde, N. Revi, S. Murugappan, S. P. Singh and A. K. Rengan, Enhanced Permeability and Retention Effect: A Key Facilitator for Solid Tumor Targeting by Nanoparticles, *Photodiagn. Photodyn. Ther.*, 2022, **39**, 102915, DOI: **10.1016/j.pdpdt.2022.102915**.

149 Y. Li, C. P. Tan, W. Zhang, L. He, L. N. Ji and Z. W. Mao, Phosphorescent Iridium(III)-Bis-N-Heterocyclic Carbene Complexes as Mitochondria-Targeted Theranostic and Photodynamic Anticancer Agents, *Biomaterials*, 2015, **39**, 95–104, DOI: **10.1016/j.biomaterials.2014.10.070**.

150 M. Zanoni, F. Piccinini, C. Arienti, A. Zamagni, S. Santi, R. Polico, A. Bevilacqua and A. Tesei, 3D Tumor Spheroid Models for in Vitro Therapeutic Screening: A Systematic Approach to Enhance the Biological Relevance of Data Obtained, *Sci. Rep.*, 2016, **6**, 19103, DOI: **10.1038/srep19103**.

151 L. C. Kimlin, G. Casagrande and V. M. Virador, In Vitro Three-Dimensional (3D) Models in Cancer Research: An Update, *Mol. Carcinog.*, 2013, **52**(3), 167–182, DOI: **10.1002/mc.21844**.

152 R. Barrera-Rodríguez and J. M. Fuentes, Multidrug Resistance Characterization in Multicellular Tumour Spheroids from Two Human Lung Cancer Cell Lines, *Cancer Cell Int.*, 2015, **15**(1), 47, DOI: **10.1186/s12935-015-0200-6**.

153 J. J. Cao, Y. Zheng, X. W. Wu, C. P. Tan, M. H. Chen, N. Wu, L. N. Ji and Z. W. Mao, Anticancer Cyclometalated Iridium(III) Complexes with Planar Ligands: Mitochondrial DNA Damage and Metabolism Disturbance, *J. Med. Chem.*, 2019, **62**(7), 3311–3322, DOI: **10.1021/acs.jmedchem.8b01704**.

154 C. A. Puckett, R. J. Ernst and J. K. Barton, Exploring the Cellular Accumulation of Metal Complexes, *Dalton Trans.*, 2010, **39**(5), 1159–1170, DOI: **10.1039/B922209J**.